



A comprehensive kinetic modeling of oxymethylene ethers (OME_n , $n=1-3$) oxidation - laminar flame speed and ignition delay time measurements



Krishna P. Shrestha^{a,*}, Sven Eckart^b, Simon Drost^c, Chris Fritzsche^b, Robert Schießl^c, Lars Seidel^d, Ulrich Maas^c, Hartmut Krause^b, Fabian Mauss^a

^a Thermodynamics and Thermal Process Engineering, Brandenburg University of Technology, Siemens-Halske-Ring 8, Cottbus 03046, Germany

^b Institute of Thermal Engineering, TU Bergakademie Freiberg, Freiberg, Germany

^c Karlsruhe Institute of Technology, Institute of Technical Thermodynamics, Engelbert-Arndold-Strasse 4, Karlsruhe 76131, Germany

^d LOGE Deutschland GmbH, Querstraße 48, Cottbus 03044, Germany

ARTICLE INFO

Article history:

Received 2 May 2022

Revised 4 October 2022

Accepted 4 October 2022

Available online 20 October 2022

Keywords:

Oxymethylene ethers

Laminar flame speed

Ignition delay time

Rapid compression machine, Kinetic

modeling

eFuel

ABSTRACT

This work reports on the development and experimental validation of a detailed reaction mechanism for the oxidation of polyoxymethylene dimethyl ethers (OME_n , $n = 1-3$). The validation is done by constant-volume chamber laminar flame speeds (393 K and 443 K, 1 to 5 bar, and equivalence ratio 0.8 to 1.6) and Rapid Compression Machine ignition delay times (550–680 K, 10 and 15 bar, equivalence ratios of 0.5–2.0) in OME_n /air mixtures. Using our new experimental and published data, the validation basis for the new kinetic model comprises the pyrolysis and oxidation of OME_n ($n = 1-3$) in freely propagating flames, auto-ignition in rapid compression machines and shock tubes, and speciation in jet-stirred and flow reactors as well as burner-stabilized premixed flames. The model provides a reasonable agreement with the experimental data for a broad range of conditions investigated. The performance of the developed model is compared against the recent literature models. OME_n ($n = 1-3$) all have the same laminar flame speed. The model suggests that the chemistry of OME_0 (DME) and CH_3OCHO (methyl formate) is the one that dictates the flame chemistry. Under the same pressure and equivalence ratio conditions, ignition delay times of OME_2 and OME_3 are similar for the investigated temperature range. This work helps to improve the understanding of OMEs chemistry. The model developed in this work will serve as the base mechanism for higher chain length OMEs ($n > 3$).

© 2022 The Combustion Institute. Published by Elsevier Inc. All rights reserved.

1. Introduction

Oxymethylene ethers (OMEs) have received attention for their prospective role as novel synthetic fuels. OMEs, with the general molecular structure $\text{CH}_3\text{O}(\text{CH}_2\text{O})_n\text{CH}_3$ ($n = 1-5$), are liquid fuels that can be used as diesel fuels. The physical and chemical properties of OME_n ($n = 2-5$) are comparable to diesel fuel (see Table 1). OME_n ($n = 2-5$) have the potential to be used immediately as drop-in fuels [1]. These fuels are of interest due to their high cetane number, high oxygen content, and an absence of C–C bonds allowing for soot-free combustion, low- NO_x emissions, and that renewable production is technically feasible. OMEs are synthesized using feedstock with end-group ($\text{CH}_3\text{O}-$) providers, such as methanol, dimethyl ether, or OME_1 , and chain-group ($-\text{CH}_2\text{O}-$) providers, such as formaldehyde, trioxane, or paraformaldehyde.

Higher chain length OMEs synthesized from smaller chain length OMEs (e.g., OME_1) are considered promising alternatives to fossil fuels, especially in compression ignition engines [2,3]. Studies on these emerging renewable alternative fuels are required to enhance our understanding.

The OME_n with $n = 1$ is dimethoxymethane (DMM), also called methylal, and is also discussed as a diesel fuel additive. Experiments have shown that DMM/diesel fuel blends require engine modifications [4]. However, OME_n with $n = 2-5$ blended with diesel fuel can be used in an engine without requiring special modifications in the engine infrastructure. Awad et al. [5] showed in their review that OME_n ($n = 2-4$) mixtures would be the optimal choice for HCCI engines in terms of cetane number, boiling points (see Table 1) and soot formation, as well as NO_x reduction without after-treatment systems. This is also backed by the study of Dworschak et al. [6], who conducted a single-cylinder diesel engine experiment using OME_n ($n = 2-5$) as neat fuel. At standard conditions compared to DME (OME_0), OME_n ($n = 2-5$) are liquid,

* Corresponding author.

E-mail address: sthakrish@gmail.com (K.P. Shrestha).

Table 1

Properties of different OMEs and diesel assembled from various sources [6,18–22].

	Diesel	OME ₀	OME ₁	OME ₂	OME ₃	OME ₄	OME ₅
Chemical formula	C ₁₂ –C ₂₀	C ₂ H ₆ O	C ₃ H ₈ O ₂	C ₄ H ₁₀ O ₃	C ₅ H ₁₂ O ₄	C ₆ H ₁₄ O ₅	C ₇ H ₁₆ O ₆
Molecular weight [g/mol]	~198–202	46	76	106	136	166	196
Density at 25°C [g/cm ³]	~0.82–0.84	0.00191855 (gas, 1 atm)	0.86	0.96	1.02	1.06	1.1
Kinematic Viscosity [mm ² /s]	2.5 – 3.2 @40°C [21]	0.184 @25°C [20]	0.318 @40°C [22]	0.559 @40°C	0.86 @40°C [6]	1.32 @40°C [6]	1.93 @40°C [6]
Melting point [°C]	–	–138	–105	–65	–41	–7	18.5
Boiling point [°C]	163–357	–35	42	105	156	202	242
Cetane number	56.5	55	29	63	78	90	100
Oxygen content [wt%]	0	34.8	42.1	45.3	47.1	48.2	49
Lower heating value [MJ/kg]	42.68	28.8	22.4	20.3	19.1	18.4	17.9
H/C ratio	~1.952	3	2.66	2.5	2.4	2.33	2.29
O/C ratio	0	0.5	0.666	0.75	0.8	0.83	0.86
AFR _{stoc} [kg/kg]	14.5	9	8.025	6.65	6.12	5.85	5.66

and their physical properties can overcome the disadvantages of OME₁ related to blending fuels (Table 1).

Recently, there have been several fundamental studies [7,8] to characterize the combustion behavior of OME_n ($n = 1$ –5). He et al. [9] performed a theoretical and experimental study and developed a detailed kinetic model to characterize the autoignition of OME₃. Similarly, Cai et al. [10] conducted a shock tube experimental study of OME_n ($n = 2$ –4) and used it to develop a kinetic model. However, both models [9,10] were not validated against other experimental data, e.g., laminar flame speed, speciation in a jet-stirred reactor, and flames. Recently, Qiu et al. [11] performed a speciation study of OME₃ oxidation in a jet-stirred reactor. They compared the He et al. [9] and Cai et al. [10] models against their experimental data and found that both models underestimated the O₂ consumption at temperatures above 800 K. Similarly, Ngugi et al. [12] conducted an experimental study of OME₂ in a shock tube (ignition delay time) and a Bunsen burner (laminar flame speed). They used the model of Cai et al. [10], Ren et al. [13], and Sun et al. [14] to reproduce their experimental data. They showed that neither mechanism could accurately reproduce their measured laminar flame speeds and ignition delay times simultaneously. Fundamental studies on the effect of blending OMEs with conventional fuels have also been carried out recently. Richter et al. [15] studied the effect of blending OME_n ($n = 3$ –5) with a diesel surrogate on sooting propensity and laminar flame speed. They found that blending OME with diesel surrogate enhanced the flame speed and decreased the sooting propensity. Further, they reported that sooting propensity was found to depend strongly on the OME_n blending grade but not on its chain length. Similarly, Ngugi et al. [16] investigated the influence of blending OME₁ with primary reference fuel (PRF) 90 on ignition delay time and laminar flame speeds. They found that blending with OME₁ shortened the ignition delay time and increased the laminar flame speed of PRF.

Experimental data on laminar flame speed for OME_n ($n = 1$ –3) at elevated pressure and temperature and ignition delay times at a temperature below 700 K are limited. The experimental database for OME_n ($n = 1$ –3) is not yet broad enough. Understanding the chemistry of short-chain OMEs forms the basis for characterizing the combustion kinetics of long-chain OMEs. There is no generally applicable kinetic model for OME_n ($n = 1$ –3) combustion, covering a broad range of experimental conditions. This identifies the need for an in-depth analysis of OME_n ($n = 1$ –3).

In our previous work [17], we investigated the interaction of NO_x with DME and DMM under combustion relevant conditions. The present work aims to extend our published mechanism [17] for predicting the combustion behavior of OME_n ($n = 1$ –3). We extended the existing validation database by laminar flame speed measurements of OME_n ($n = 1$ –3) at elevated pressures and temperatures. To obtain data relevant for the low-temperature chemistry of OME, we conducted ignition delay time measurements of

OME₂ and OME₃ in a Rapid Compression Machine (RCM); these data include previously not reported conditions, 10 bar and 15 bar, 550 – 680 K, equivalence ratios of 0.5 – 2.0. Relevant studies on the combustion behavior of OME_n ($n = 1$ –3) are compiled in Table 2. The literature data are limited for neat OME_n ($n > 1$). More experimental and theoretical works are required for a deeper insight into the oxidation behavior of OMEs.

In this study, we adopted a similar strategy as described in our previous work [13,14] for the construction of a robust kinetic model for combustion modeling applications. In this work, we have developed a comprehensive kinetic model for OME_n ($n = 1$ –3) by thoroughly validating the model against a large experimental data pool compiled in Table 2, i.e., laminar flame speeds (LFS), ignition delay times (IDT), speciation in jet-stirred reactors (JSR), flow reactor (FR) and burner stabilized flames (BSF). This work is part of an ongoing effort to develop a reliable and comprehensive mechanism for OME_n ($n = 1$ –5).

2. Experimental details

2.1. Constant volume chamber

The laminar flame speed (LFS) measurements were conducted at TU Bergakademie Freiberg using a constant volume chamber (CVC). The CVC has an inner diameter of 100 mm and is equipped with two orthogonal pairs of quartz windows of 45 mm diameter. The technical construction of the test rig, acquisition, experimental uncertainties, and data analysis are described in Rau et al. [31] and Eckart et al. [32]. The fuel-air mixtures were prepared in the vessel according to the required partial pressures of the gaseous components. The flame images are captured by schlieren photography with a Photron Fastcam SA1.1 with a frame rate of 10,000 frames per second at a resolution of 768 × 768 pixels. The current pixel/length ratio is 177 pixels/cm or 0.056 mm/pixel. The laminar flame speed is derived based on the non-linear approach for a flame radius above 10 mm [33] and below 0.75 times (34 mm) [34] of the chamber radius. Further, the uncertainties for initial temperature are ±2 K and initial pressure ±0.05 bar, respectively.

The experiments of all three OME_n ($n = 1$ –3) were conducted under the same initial conditions, i.e., $T_u = 393$ –443 K, $P_u = 1$, 3, and 5 bar, and equivalence ratios of 0.8–1.4. For some higher equivalence ratios and pressures, the expected cellularity emerged. Therefore, the LFS of the CVC method is based on averaged values from at least five individual measurements without cellular flames. The uncertainty bars of the LFS measurements with the CVC correspond to the standard deviation of these different values, following the uncertainty evaluation of Rau et al. [31]. Chen [34] and Konnov et al. [35] reviewed the methane LFS measurements with the CVC method and showed deviations in the range of 3 – 8 cm/s

Table 2Summary of experimental studies pertinent to OME₂ and OME₃ oxidation*.

Case	Experimental devices	Measured properties	Experimental conditions	Refs.
OME₂				
1	Constant volume chamber	LFS ¹	1 – 5 bar, 393 and 443 K, $\phi = 0.6 - 1.9$ for OME ₂ /air	This work
2	Heat flux burner	LFS	1 bar, 380 – 401 K, $\phi = 0.6 - 1.9$ for OME ₂ /air	Eckart et al. [23]
3	Nozzle - Conical-shaped flame	LFS	1, 3 and 6 bar, 473 K, $\phi = 0.5 - 2.0$ for OME ₂ /air	Ngugi et al. [12]
4	Shock tube	LFS	1, 4 and 16 bar, 850 – 1700 K, $\phi = 1$ for OME ₂ /O ₂ /N ₂	Ngugi et al. [12]
5	Shock tube	IDT ²	10 and 20 bar, 663 – 1112 K, $\phi = 0.5 - 2$ for OME ₂ /air	Cai et al. [10]
6	RCM	IDT	3 – 10 bar, 570 – 690 K, $\phi = 1.0$ for OME ₂ /air	Drost et al. [24]
7	RCM	IDT	10 bar, 600 – 715 K, $\phi = 0.5$ for OME ₂ /air	Ras et al. [25]
8	RCM	IDT	10 and 15 bar, 550 – 680 K, $\phi = 0.5$ and 2.0 for OME ₂ /air	This work
9	Flow reactor	Speciation	1 atm, 750 – 1250 K, $\phi = 0.8, 1.2$ and 2.0 for OME ₂ /O ₂ /Ar	Gaiser et al. [26]
10	Flow reactor (py ³)	Speciation	3.4 bar, 373 – 1073 K, $\phi = \infty$ for OME ₂ (0.3 μ l)/He (92 Nml/min)	Ras et al. [25]
11	Flow reactor (py)	Speciation	1.5 bar, 850 – 1150 K, $\tau = 400 - 850$ ms, $\phi = \infty$ for OME ₂ /N ₂	Ras et al. [27]
12	Burner stabilized flame	Speciation	40 mbar, 273 K, $\phi = 1.7$, $T_{ad} = 2452$ K for OME ₂ /O ₂ /Ar	Gaiser et al. [28]
13	Jet-stirred reactor (py)	Speciation	1.03 atm, 450 – 1080 K, $\phi = \infty$ for OME ₂ /Ar (99%)	Zhong et al. [29]
OME₃				
14	Constant volume chamber	LFS	1 and 3 bar, 393 and 443 K, $\phi = 0.8 - 1.6$ for OME ₃ /air	This work
15	Constant volume combustion vessel	LFS	1 atm, 363 – 423 K, $\phi = 0.7 - 1.8$ for OME ₃ /air	Wang et al. [30]
16	Constant volume cylindrical combustion vessel	LFS	1 atm, 408 K, $\phi = 0.7 - 1.6$ for OME ₃ /air	Sun et al. [14]
17	Shock tube	IDT	10 and 20 bar, 684 – 1137 K, $\phi = 0.5 - 2$ for OME ₃ /air	Cai et al. [10]
18	RCM	IDT	15 bar, 550–680 K, $\phi = 0.5$ for OME ₃ /O ₂ /CO ₂	This work
19	RCM	IDT	15 bar, 550–680 K, $\phi = 2$ for OME ₃ /air	This work
20	RCM	IDT	3 – 10 bar, 570 – 690 K, $\phi = 1.0$ for OME ₃ /air	Drost et al. [24]
21	RCM	IDT	10 and 15 bar, 640–865 K, $\phi = 0.5 - 1.5$ for OME ₃ /O ₂ /N ₂	He et al. [9]
22	Flow reactor	Speciation	1 atm, 750 – 1250 K, $\phi = 0.8, 1.2$ and 2.0 for OME ₃ /O ₂ /Ar	Gaiser et al. [26]
23	Jet-stirred reactor	Speciation	1 atm, 500 – 950 K, $\phi = 0.5 - 2.0$ and $\tau = 2$ s for OME ₃ /O ₂ /N ₂	Qiu et al. [11]
24	Jet-stirred reactor (py)	Speciation	1.03 atm, 450 – 1080 K, $\phi = \infty$ for OME ₃ /Ar (99%)	Zhong et al. [29]
25	Burner stabilized flame	Speciation	40 mbar, 273 K, $\phi = 1.7$, $T_{ad} = 2452$ K for OME ₃ /O ₂ /Ar	Gaiser et al. [28]
26	Burner stabilized flame	Speciation	33.33 mbar, 273 K, $\phi = 1$ for OME ₃ /O ₂ /Ar (50%)	Sun et al. [14]

* For a literature compilation of OME₁, see Shrestha et al. [17].¹ LFS: laminar flame speed.² IDT: ignition delay time.³ py: pyrolysis.

and 5 cm/s respectively. In our previous work, we compared the measurements from the constant volume chamber against the heat flux burner [31,32] under atmospheric conditions, and a reasonable consistency between both setups was found. This result is in good agreement with the findings of Konnov et al. [35]. The Markstein length, L_b was calculated for OME_n ($n = 1-3$) as described in Li et al. [36].

2.2. Rapid compression machine

The ignition delay times presented in this work were measured in a Rapid Compression Machine (RCM) at Karlsruhe Institute of Technology. The RCM, a piston-cylinder device for the compression of gases, is described in more detail elsewhere [37] and is validated with liquid fuels in [38]. In an RCM experiment, the desired OME_n/air mixture was produced from pure substances using the partial pressure method. The gases O₂, N₂, and CO₂ (purity of 99.995%, 99.999%, and 99.995%, respectively) and fuel (OME₂ and OME₃, purity 0.988% or 0.99%, respectively) were filled into a mixing chamber with a volume of 10 liters. The fuel-air mixture from the mixing chamber was admitted into the RCM combustion chamber. The used sensors are absolute pressure transmitter MKS 121A Baratron supplied by MKS Instruments Inc., Andover, MA 01810, USA with an accuracy of $\leq \pm 0.5\%$ of reading; cylinder pressure sensor Kistler 6061 B supplied by Kistler Gruppe, 8408 Winterthur with linearity of $\leq 0.5\%$. The combustion chamber, the pipes, the mixing chamber, and sensors were heated to at least 373 K to avoid condensation. After the filling procedure, the piston was pneumatically pushed into the cylinder, thus compressing the gas (compression time approx. 30–40 ms). A mechanical lock was used to stop the piston at the top dead center (TDC).

After the end of compression (EOC), which is defined as time 0, the IDT was detected via the chemistry-induced pressure increase. The pressure associated with the experiment was defined as the pressure at the end of compression, P_{EOC} . The associated temperature T_{EOC} was determined from the pressure at TDC using the adiabatic core assumption [39]. Based on the accuracies for the pressure measurements, the uncertainty in the compression pressure is approx. ± 0.15 bar. A numerical error propagation analysis is performed to find the uncertainty in the compression temperature. With the uncertainties of each input variable, Gaussian probability density functions (PDFs) are calculated. For the mentioned conditions, the uncertainty of compression temperature is approx. ± 8 K. Fig. 1 shows two measured pressure curves with OME₂. After compression, both pressure curves reach a pressure of approx. $P_{EOC} = 15$ bar (end of compression is shifted to time 0). The reactive mixture (solid line) ignites at about 135 ms, which is measured by a sharp increase in pressure. The non-reactive mixture (dashed line) does not ignite because O₂ is replaced by the same amount of N₂.

3. Chemical kinetic modeling

The mechanism proposed here extends our previous work (Shrestha et al. [17]), which was developed to predict dimethyl ether (OME₀) and dimethoxymethane (OME₁) oxidation and its interaction with NO_x chemistry. This mechanism [17] was validated for C₁-C₂ fuels, e.g., methane (CH₄), acetylene (C₂H₂), ethylene (C₂H₄), ethane (C₂H₆), methanol (CH₃OH), acetaldehyde (CH₃CHO), and ethanol (C₂H₅OH), over a wide range of experimental conditions. It has been demonstrated that the kinetic model satisfactorily captured the oxidation kinetics of C₁-C₂ hydrocar-

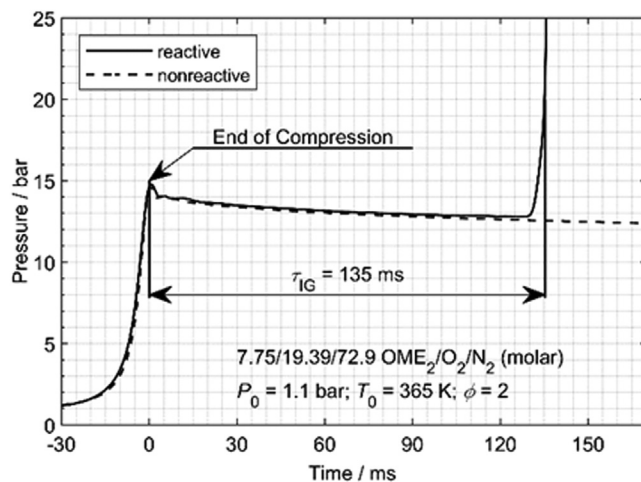
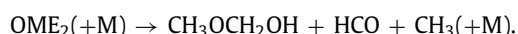


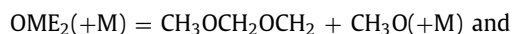
Fig. 1. Measured pressure curves in the RCM for a reactive, fuel-rich OME₂ mixture (solid line) and the corresponding non-reactive mixture (dashed line).

bon/oxygenated and their interaction with NO_x. The mechanism is constructed hierarchically. The model also includes detailed NO_x chemistry, which stems from our previous work [17], and can be used for NO_x predictions and modeling. The OME₂ and OME₃ sub-mechanism is based on the modeling work of He et al. [9]. Their work [9] primarily focused on OME₃ autoignition timing modeling. Their model also included OME₂ as a sub-set. We note here that He et al. [9] validated their model only of OME₃. Implementing their OME₂ and OME₃ sub-model in our mechanism without any changes did not provide a satisfactory result against the experimental data for OME₂ and OME₃, specially IDT and speciation in JSR. One of the reasons is due to different base chemistry. He et al. [9] constructed the OME₃ mechanism based on the work of Burke et al. [40]. They [9] adopted the OME_n ($n = 1-3$) high-temperature chemistry from Sun et al. [14], which they further extended by adding the low-temperature chemistry of these fuels. Our base mechanism was developed over the past five years [17,41–46]. In this study, we have updated OME₂ and OME₃ sub-mechanism as it was necessary to cover a wide range of experimental conditions (Table 2).

Here, we briefly discuss the updated reactions in this work, starting with OME₂ related reactions. He et al. [9] included only four unimolecular decomposition paths for OME₂. In this work, we added two more reactions which are:



The rate parameter of these reactions is adopted from Zhong et al. [29]. Further, the rate constants of reactions



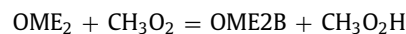
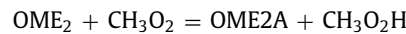
were adopted with an analogy to reactions of diethoxymethane (DEM):



respectively from the modeling work of Zhang et al. [47]. The inclusion of new reactions and updates on rate parameters improved

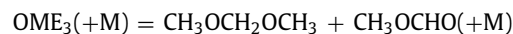
the model performance for pyrolysis conditions of OME₂ (see Fig. 2 and Figs. S1–3 in the supplementary material (SM), cases 13 and 24 in Table 2). Very recently, Ras et al. [27] conducted an experimental and modeling study on the pyrolysis of OME₂. Their study suggested that carbene is also formed via unimolecular decomposition of fuel which quickly decomposes as they are highly unstable. They stated that including carbene chemistry improved their model performance for predicting OME₂ pyrolysis at high temperatures. We note here that during the time the present work was conducted, the work of Ras et al. [27] was not yet published, and those new findings could not be taken into account in our model. Regardless of that, the present model of this work can nicely predict the OME₂ pyrolysis.

The rate constant of H-abstraction reaction from OME₂ by HO₂, CH₃, and CH₃O is adopted from the modeling work of Cai et al. [10]. The rate parameter of the H-abstraction reaction



are adopted with an analogy to reaction DMM + CH₃O₂ from our previous work [17]. The H-abstraction reactions by CH₃O and CH₃O₂ are sensitive in predicting the ignition delay time in the NTC region, and updating the rate constant improved the model performance.

Similarly, in the OME₃ sub-mechanism, He et al. [9] included only five unimolecular decomposition channels of OME₃. In this work, we have added additionally four new reactions for OME₃ thermal decomposition, which are:



The rate parameter of these reactions is adopted from Zhong et al. [29]. Further, the rate parameter of the reaction



is adopted with an analogy to DEM = C₂H₅OCH₂O + C₂H₅ and DEM = C₂H₅OCH₂ + C₂H₅O, respectively, from the modeling work of Zhang et al. [47]. The inclusion and update of the above reactions improved the model predictions for pyrolysis of OME₃ (see Fig. 2 and Figs. S1–3 in SM). Fig. 2 depicts the literature model performance against the pyrolysis experiment from Zhong et al. [29] for fuel decomposition. We can observe that for OME₁ all models perform satisfactorily. However, for OME₂ and OME₃ Cai et al. [10] and He et al. [9] model perform worse, while Ras et al. [25] model performs alike to our model for OME₂. Zhong et al. [29] also compared the Cai et al. [10] and He et al. [9] model performance against their experimental pyrolysis data for OME_n ($n = 1-3$) and reached a similar conclusion. Our work mainly focuses on characterizing the oxidation behavior of these fuels; however, the proposed model is also able to predict the experimental pyrolysis data. He et al. [9] did not include the H elimination reaction from OME₃,



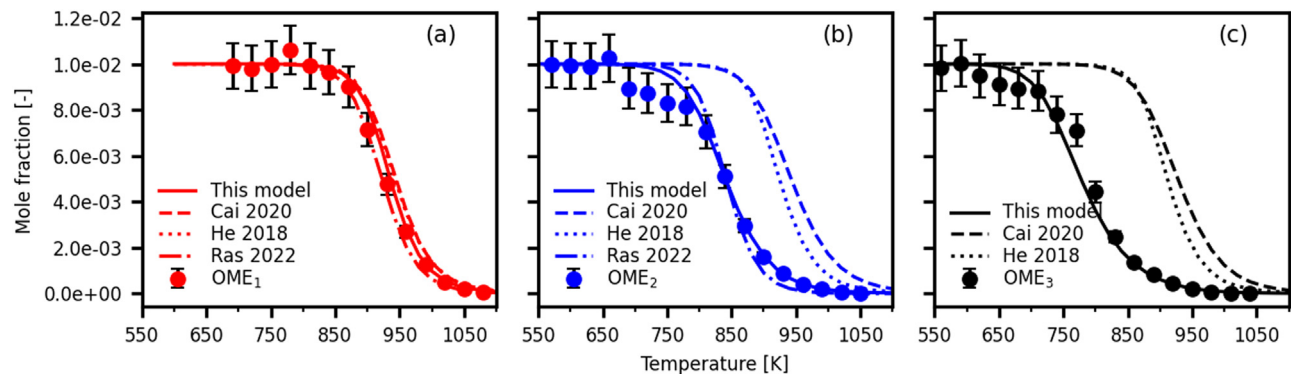
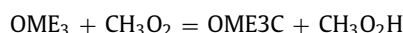
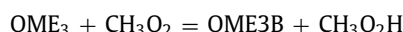
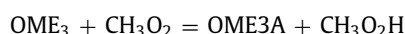
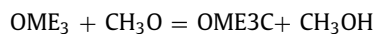
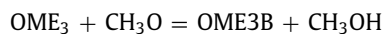
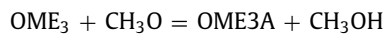


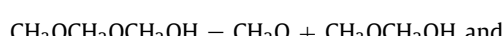
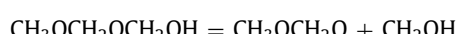
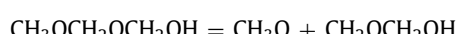
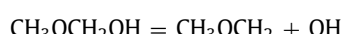
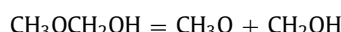
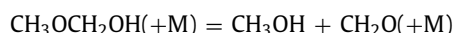
Fig. 2. OME₁ (a), OME₂ (b), and OME₃ (c) pyrolysis with Ar bath gas in a jet-stirred reactor at 1 atm, $\tau = 2$ s. Symbols: experimental data from Zhong et al. [29], Lines: model predictions; solid lines: this model, dashed lines: Cai et al. [10], dotted: He et al. [9], and dash-dotted lines: Ras et al. [25].



In this work, we have included these reactions adopting the rate parameter from Cai et al. [10]. The rate constant of H-abstraction reaction from OME₃ by CH₃O and CH₃O₂,



is adopted from the modeling work of Cai et al. [10]. These reactions are very sensitive for ignition delay time predictions of OME₃ at the NTC regime. The update in the rate parameter of these reactions improved the model performance in our work. Furthermore, unimolecular decomposition paths of CH₃OCH₂OH and CH₃OCH₂OCH₂OH were added, adopting the rate parameter from Zhong et al. [29]. These species are formed from the thermal dissociation of OME₃. The added reactions are



In addition to the above update, we updated the rate parameter of reaction C₂H₅ + HO₂ = C₂H₄ + H₂O₂ and C₂H₅ + HO₂ = C₂H₅O + OH adopting the rate parameter from the experimental study of Ludwig et al. [48] on C₂H₅ + HO₂ system

which improved the C₂H₄ formation in jet-stirred reactor conditions for investigated fuels.

Thermodynamic data of the species in OME₂ and OME₃ sub-mechanisms are also adopted from He et al. [9]. However, the transport properties of the species were not available. Therefore, in this work, we have compiled the transport properties of the species included in the OME₂ and OME₃ sub-mechanism, adopting from various literature sources or estimates. 86 species and 297 reactions have been added. The complete mechanism consists of 259 species and 1678 reactions in CHEMKIN format and can be found in the supplementary material.

To note here that to access the impact of model extension in this work (OME₂ and OME₃) on OME₀, we again validated our model against the previous experimental target (compiled in Shrestha et al. [17]). The extensive model validation of OME₀ can be found in the supplementary material.

4. Results and discussion

The symbols in the figures are experimental data from this work or the literature, and the lines are model predictions unless otherwise stated. The performance of different published kinetic models are also assessed. Three literature models are chosen, which are Cai et al. [10], He et al. [9], and Ras et al. [25], and hereafter, we call them as Cai model, He model, and Ras model, respectively. The Cai model is the only one that provides transport properties of species and includes all fuels we have investigated in this study. Therefore, laminar flame speed simulations are only possible with the Cai model. Similarly, Ras et al. [25] did not consider OME₃ as a fuel in their work; therefore, only simulations of OME₁ and OME₂ were performed. Table S2 in the supplementary material provides information on the simulation results of different models. Simulations are performed with the software HOMREA [49] for RCM ignition delay time, and all other simulations were performed using LOGEresearch v1.14 [50].

4.1. Influence of initial pressure and equivalence ratio on flame morphology

The effects of initial pressure and equivalence ratio on the destabilization of the flame front have been investigated. Fig. 3 shows a series of snapshots of OME₂/air flames with an initial pressure of $P_u = 3$ and 10 bar and an equivalence ratio (ϕ) of 0.8–1.4. The combustion duration times differ for each image as the propagation speed is also different. The figure shows the development of the flames with the largest possible radius, and the tendency to cellular formation increases with increasing equivalence ratio. For the leanest mixture, $\phi = 0.8$, the flames in the aforementioned radius are smooth. In other cases, it can be noticed that

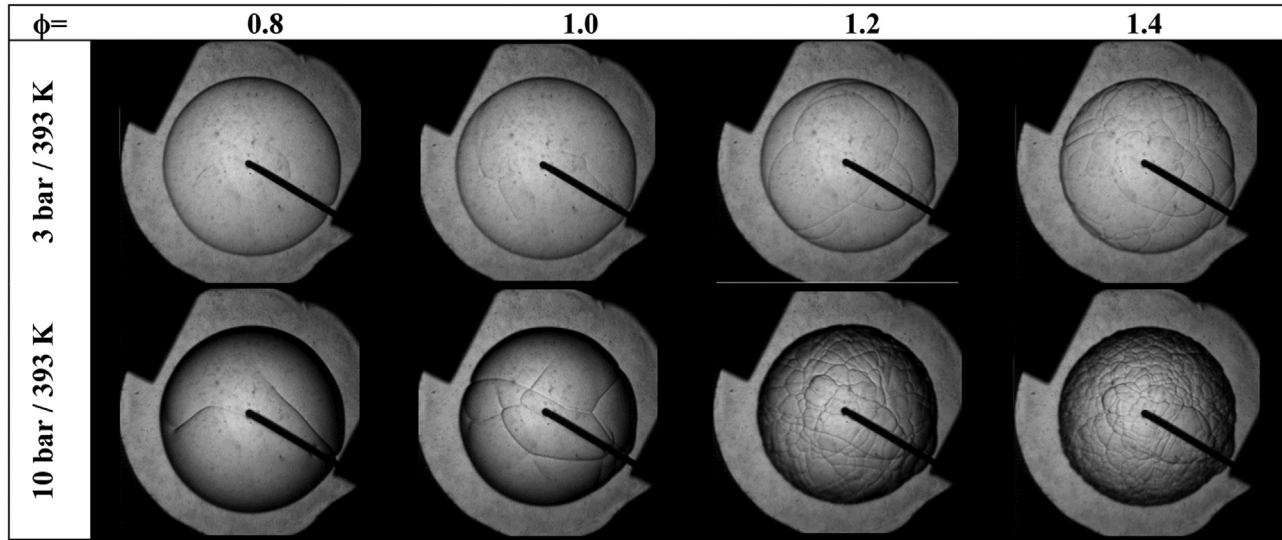


Fig. 3. Flame morphology of OME₂/air for $\phi = 0.8\text{--}1.4$ at $T_u = 393\text{ K}$ and $P_u = 3$ and 10 bar; the radius of spherical flame fronts $r \sim 1.4\text{ cm}$.

hydrodynamic instabilities in the shape of small cells and thermo-diffusive instabilities in the form of cracks start increasing as pressure increases and the mixture gets richer. The acceleration caused by the cellularities contradicts the theory, so in this case, flames above $\phi = 1.4$ for 3 bar were no longer used to consider the laminar flame speed. Especially at higher pressures, the ranges of the images to be evaluated narrow down further and thus also influence the effect of the extrapolation. In the rich mixtures above $\phi = 1.4$, cellularities frequently occur so that they cannot be used to assess the propagation speed of the flames. In the lean range, significant ignition effects occur in the measurements, especially at higher pressures, and the expression of cracks could be observed. For these reasons, only a limited dataset can be presented, and to ensure the high quality of the data, images showing cellularity were not used for the analysis.

4.2. Laminar flame speed

Figure 4 displays the laminar flame speeds of OME₁/air at $P_u = 1$ bar and temperature range, $T_u = 298\text{--}443\text{ K}$, as a function of the equivalence ratio. Literature data [17,23] (Fig. 4a), own measurements (Fig. 4b), and model predictions from this work (solid lines) and Cai et al. [10] (dashed lines) are shown. Our model captures the experimental data at 1 bar for the whole range of investigated equivalence ratios, whereas the Cai model slightly underpredicts at rich conditions ($\phi > 1.6$). At 443 K and both 1 and 3 bar (Fig. 4b), the maximum LFS is retained at $\phi = 1.1$ as observed for other conditions in Fig. 4a. At 3 bar as well, our model excellently captures the measured laminar flame speed. The performance of Cai model is also comparable to our model.

Similarly, Fig. 5 displays the laminar flame speed of OME₂/air at $T_u = 393\text{ K}$ for pressure $P_u = 1\text{--}5$ bar (Fig. 5a) and $T_u = 443\text{ K}$ for pressure $P_u = 1\text{--}3$ bar (Fig. 5b). At 1 bar for both temperatures, the model captures the experimental data for the whole range of investigated equivalence ratios ($\phi = 0.6\text{--}1.9$). However, at 3 and 5 bar for $\phi = 0.9\text{--}1.2$, our model slightly underpredicts the laminar flame speed, which is also true for the Cai model. For instance, at $\phi = 1.1$ and 393 K, our model underpredicts the experimental data by 8.7% and 13.6% for 3 and 5 bar, respectively. However, at 443 K and 3 bar the model underpredicts the flame speed by 6.3%. Further, Cai model also performs alike our model for whole range of investigated conditions. Model predictions are in good agreements with experiments in lean and rich conditions ($\phi > 1.1$). We

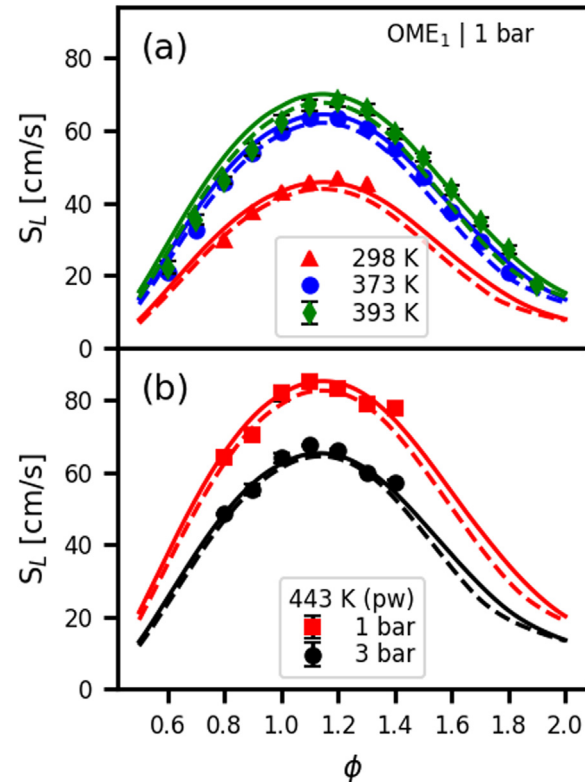


Fig. 4. OME₁/air laminar flame speed at initial mixture pressure of 1 and 3 bar, and temperature of 298 – 443 K. Symbols: experiments (a) previous work [17,23], (b) present work (pw). Solid lines: model predictions from this work, dashed lines: Cai et al. [10] model predictions.

note that we do not want to optimize the model to match laminar flame speed only. The developed model is validated against the broad range of experimental conditions from different reactor setups (Table 2 and Table S2 in SM).

Figure 6 shows our model (solid lines) and Cai model (dashed lines) comparison against the present and literature laminar flame speed experimental data for OME₃/air mixture for various temperatures at $P_u = 1$ and 3 bar. Both models can capture most of the experimental data and follows the trend very well. However, both

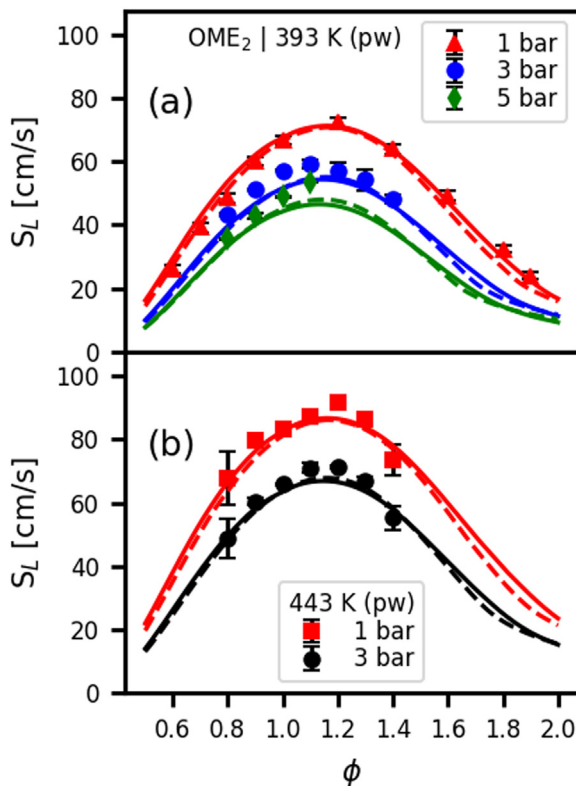


Fig. 5. OME₂/air laminar flame speed at initial mixture pressure of 1, 3, and 5 bar, and temperature of 393 and 443 K. Symbols: present experimental work (a) $T_u = 393$ K, (b) $T_u = 443$ K. Solid lines: model predictions from this work, dashed lines: Cai et al. [10] model predictions.

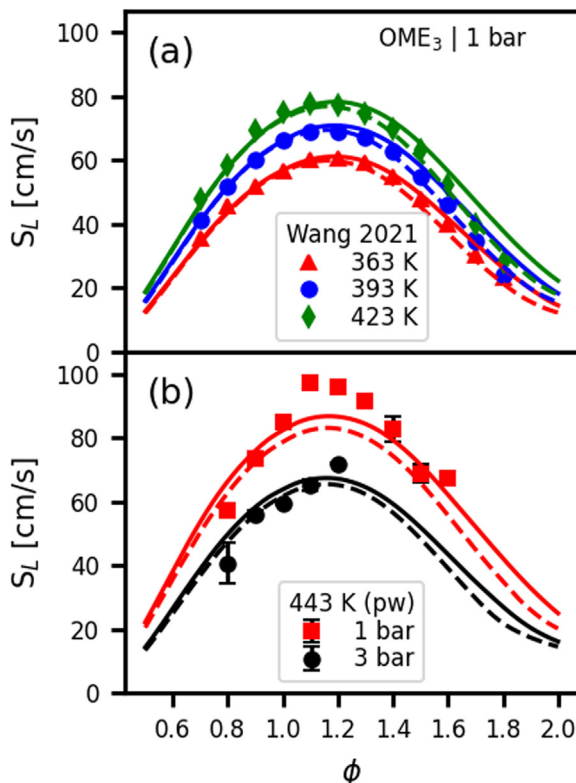


Fig. 6. OME₃/air laminar flame speed at initial mixture pressure of 1 and 3 bar, and temperature of 363 - 443 K. Symbols: experiments, (a) literature work [30], (b) present work. Solid lines: model predictions from this work, dashed lines: Cai et al. [10] model predictions.

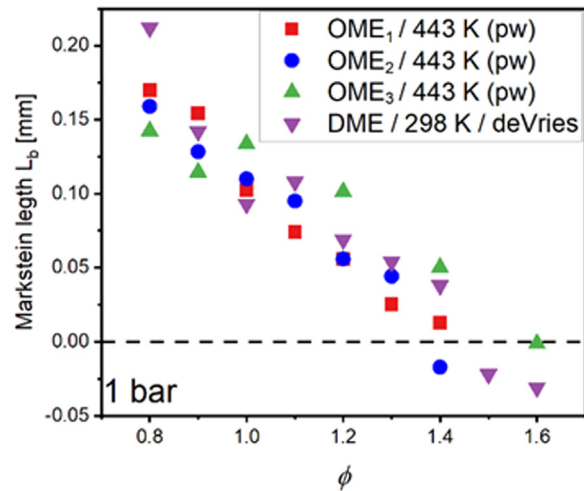


Fig. 7. Markstein lengths as a function of equivalence ratio for OME₁, OME₂, and OME₃ at 1 bar and 443 K with comparative data from de Vries et al. [53] (298K) for OME₀ (DME).

model unpredicts the present experimental data at 1 bar and 443 K for $\phi = 1.1\text{--}1.3$.

As discussed above, in Section 4.1, at rich conditions ($\phi > 1.4$) with increasing pressure flame instability due to cracks started to increase. Therefore, at higher pressure and $\phi > 1.4$ laminar flame speed data were not reliable and are not reported in this study.

Further, as expected for OME₁, OME₂, and OME₃ (Figs. 4–6), increasing the initial temperature elevates the LFS and vice versa with pressure. The increase in initial mixture temperature and pressure enhance the combustion, increasing the adiabatic flame temperature, which is consistent with our recent study [46]. Increased pressure primarily improves the combustion intensity by increasing the mixture density, though pressure also affects species diffusion and chemical kinetics through pressure dependent third-body reactions. It enhances the reaction rates of reactions that are weakly dependent on or even independent of temperature [51]. However, the increase in pressure suppresses the formation of radicals, leading to a decrease in flame speed [52]. The measured experimental data in this work for OME₁, OME₂, and OME₃ is provided in Table S3 with their respective uncertainty in the supplementary material.

Figure 7 shows the calculated Markstein length (L_b) for OME_n ($n = 1\text{--}3$) compared to de Vries et al. [53] for OME₀ (DME). For fuel-lean mixtures, the L_b are positive but become steadily smaller with increasing ϕ . The zero point for OME_n ($n = 0\text{--}2$) is reached slightly earlier than for OME₃. This means that the influence of flame stretching on flame speed is approximately equivalent for all three fuels. The changeover from stable to unstable flame occurs at a comparable equivalence ratio. Furthermore, the similarity in L_b is supported by laminar flame speed measurements (Fig. S5 in SM, cases 1 and 14 in Table 2), predicted adiabatic flame temperature, and modeling work (Section 4.3). It is also worth noting that the mechanism extension in this work (inclusion of OME₂ and OME₃ sub-models) did not impact the model predictions for OME₀ and OME₁. The calculated L_b is also provided in Table S4 in the supplementary material.

4.3. Kinetic analysis of flame

In our previous experimental and modeling work [17], we showed that the LFS of OME₀ and OME₁ are the same at $P_u = 1$ bar, $T_u = 298$ and 373 K, and $\phi = 0.6\text{--}1.8$. Here, we compare the LFS of investigated OME₁, OME₂, and OME₃ to find the impact of

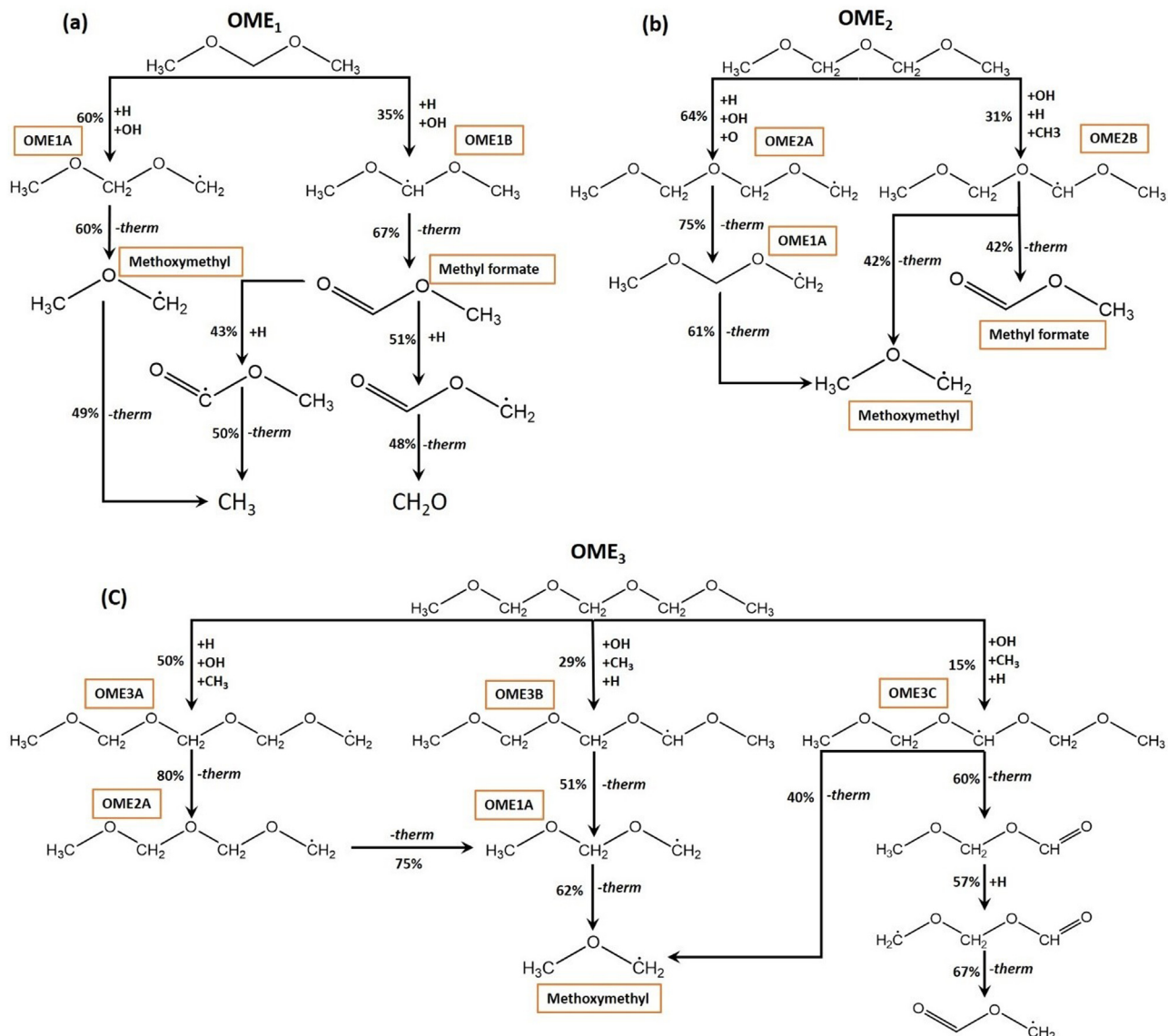


Fig. 8. Integrated mass flux analysis based on C-atom of OME₁ (a), OME₂ (b), and OME₃ (c) during the oxidation in flame at $\phi = 1.1$, $T_u = 443$ K, and $P_u = 1$ bar.

increasing the oxymethylene ($\text{CH}_2\text{--O}$) group at $T_u = 443$ K and $P_u = 1$ and 3 bar, respectively. It is found that at both pressures, OME_n ($n = 1\text{--}3$) have a similar LFS for the whole range of investigated equivalence ratios (Fig. S5 in SM, cases 1 and 14 in Table 2). This is supported by the model predicted adiabatic flame temperature of these fuels. For the entire range of investigated equivalence ratios, the adiabatic flame temperature of OME_n ($n = 1\text{--}3$) is the same (within a 5 K difference, see Fig. S5 in SM). The model further reveals that the formation of the key radicals H, OH, and O are almost the same. The only notable difference is the H-atom at $\phi > 1.2$, whose concentration increases as $\text{CH}_2\text{--O}$ length increases from OME₁ to OME₂ (Fig. S5 in SM). However, the difference in H-atom concentration is not significant as the $\text{CH}_2\text{--O}$ group further increases from OME₂ to OME₃. From the above analysis, we can conclude that the influence of the $\text{CH}_2\text{--O}$ group on the LFS on these ethers is insignificant regardless of the chain length.

To get a closer insight into the chemistry of these fuels, a reaction flow analysis is performed using here developed model at $\phi = 1.1$, $T_u = 443$ K, and $P_u = 1$ bar, shown in Fig. 8 (only major paths are shown) and discussed accordingly. OME₁ (Fig. 8a) and OME₂ (Fig. 8b) predominately undergo H-atom abstraction from α

and β sites by H-atom and OH radicals. Similarly, OME₃ (Fig. 8c) undergoes H-atom abstraction from α , β , and γ sites by H-atom, OH, and CH₃ radicals. The dominant one is the H-atom. In all these ethers, the H-abstraction from the terminal carbon atom (β for OME₁ and OME₂ while γ for OME₃) is the most favored path, and the H-abstraction from the α site is the least favored. Decomposition of the primary fuel radicals OME1A ($\text{CH}_3\text{OCH}_2\text{OCH}_2\cdot$) and OME1B ($\text{CH}_3\text{OCHOCH}_3\cdot$) of OME₁ gives methoxymethyl radical ($\text{CH}_3\text{OCH}_2\cdot$) and methyl formate ($\text{CH}_3\text{OCHO}\cdot$) as a primary product (Fig. 8a). The former is the primary fuel radical, while the latter is the intermediate during oxidation of OME₀. The formed CH_3OCH_2 mainly undergoes thermal dissociation to yield CH_3 and CH_2O . Similarly, CH_3OCHO undergoes H abstraction by H-atom from methyl and formate group, which eventually leads to CH_3 and CH_2O .

During OME₂ oxidation (Fig. 8b), the primary fuel radical OME2A ($\text{CH}_3\text{OCH}_2\text{OCH}_2\text{OCH}_2\cdot$) at the β site undergoes unimolecular dissociation to yield OME1A (a primary fuel radical of OME₁) and CH_2O . In contrast, the radical at α site OME1B ($\text{CH}_3\text{OCH}_2\text{OCHOCH}_3\cdot$) undergoes a unimolecular dissociation yielding CH_3OCH_2 (a primary fuel radical of OME₀) and CH_3OCHO .

Similarly, during the oxidation of OME_3 , the depletion of the primary fuel radical at the γ site (OME3A), which undergoes unimolecular dissociation, leads to the OME2A (a primary fuel radical of OME_2) and CH_2O . The primary fuel radical at the β site (OME3B) yields OME1A (a primary fuel radical of OME_1) and CH_3OCHO via unimolecular dissociation. The primary fuel radical at the α site (OME3C) exclusively undergoes a unimolecular dissociation to yield CH_3OCH_2 (primary fuel radical of OME_0) and $\text{CH}_3\text{OCH}_2\text{OCHO}$ (methoxymethyl formate). The reaction flow analysis suggests that at an early stage of a longer chain OME_n oxidation, there is primary fuel radical formation of the one chain length shorter OME , i.e., OME_{n-1} ($\text{OME}_3 > \text{OME}_2 > \text{OME}_1 > \text{OME}_0$), which further decomposes to one chain length shorter OME (i.e., OME_{n-2}) primary fuel radical. Regardless of their chain length, they mainly share the same chemistry of the smallest ether, OME_0 , and the simplest ester, CH_3OCHO , at an early stage of their decomposition. Further, the model reveals that for the investigated OME s, the dominant path to form hydrocarbons larger than C_2 is the recombination of CH_3 radical, leading to C_2H_6 and other higher hydrocarbons. The CH_3 radical is mainly formed via the unimolecular decomposition of the CH_3OCH_2 and CH_3OCO radicals. This analysis supports our findings from previous [17] and this study on observing the same laminar flame speed of OME_n ($n = 0-3$) regardless of their chain length.

Furthermore, Fig. 9 shows the reactions sensitivity analysis toward laminar flame speed at $\phi = 0.8$, 1.0 and 1.4, $T_u = 443$ K, and $P_u = 3$ bar for OME_1 (a), OME_2 (b), and OME_3 (c). It can be observed in Fig. 9 that for OME_n ($n = 1-3$), most of the sensitive reactions stem from the base H_2/CO chemistry. As expected, the top most sensitive reaction is the chain branching reaction $\text{H}+\text{O}_2=\text{OH}+\text{O}$, whose sensitivity decreases as the CH_2-O chain length increases. Further, with the increase of the equivalence ratio, the sensitivity of this reaction increases. Further, most of the reactions involving CO and HCO sensitivity increases with the increase of CH_2-O chain length from OME_1 to OME_3 . The chain branching ($\text{H}+\text{HO}_2=\text{OH}+\text{OH}$) and terminating ($\text{H}+\text{HO}_2=\text{H}_2+\text{O}_2$) show positive and negative sensitivity coefficients, respectively. Interestingly the pressure dependent reaction $\text{CH}_3+\text{H}(\text{+M})=\text{CH}_4(\text{+M})$ exhibits negative sensitivity, whereas the reaction $\text{C}_2\text{H}_4+\text{H}(\text{+M})=\text{C}_2\text{H}_5(\text{+M})$ shows positive sensitivity. The former reaction yields stable CH_4 while later yields radical C_2H_5 . This may explain the negative and positive sensitivity of these reactions. Further, the important pressure dependent reaction $\text{H}+\text{O}_2(\text{+M})=\text{HO}_2(\text{+M})$ shows a negative sensitivity as it consumes a very reactive H radical and produces a less reactive HO_2 radical. The sensitivity of this reaction decreases as equivalence increases. This can be explained by the less O_2 available in rich conditions compared to lean conditions. Similar observations can be made for other reactions. The common top sensitive reactions of OME_1 , OME_2 , and OME_3 further support the flux analysis (Fig. 8). Further model validation against the laminar flame speed of OME_1 , OME_2 , and OME_3 can be found in the supplementary material (Figs. S8–S11, cases 2, 3 and 16 in Table 2).

4.4. Ignition delay times

Figures 10 and 11 show IDTs measurements of OME_2 and OME_3 , respectively in the temperature range ($T_{EOC} = 588 - 696$ K), for lean ($\phi = 0.5$), stoichiometric ($\phi = 1$) and fuel-rich ($\phi = 2$) conditions obtained in RCM experiments. The IDTs for OME_3 and lean conditions were relatively short, using N_2 as diluent even at the lowest possible initial temperature and compression ratio (less OME_3 in the mixture resulted in a higher heat capacity ratio (c_p/c_v), and thus higher compression temperatures). To expand the measurable range, CO_2 as an inert gas with a low heat capacity ratio was used to lower the compression temperatures (T_{EOC}).

Measured ignition delay times (symbols) shown in Figs. 10a and 11a at $\phi = 1.0$ and 10 bar are from previous work [24], while the remaining data points are the present measurements.

Figure 10 shows the temperature dependence of OME_2 ignition delay time. Simulation results are displayed using the present model and three different models from the literature. Comparing the experimental data, it is found that the ignition delay time of the lean mixture is longer than the fuel-rich mixture. All the model follows the observed trend very well. However, for the condition at 10 bar and $\phi = 1$ (Fig. 10a), all models over predict the IDT at a temperature below 625 K. In contrast, all models underpredict for 15 bar $\phi = 1$ (Fig. 10c). For 15 bar and $\phi = 1$ (Fig. 10d) it can be observed our model predictions are similar to He model, however, Cai model under predicts the IDT.

Similarly, Fig. 11 compares the model predictions against the experimental data of OME_3 . As observed for OME_2 , a lean mixture of OME_3 also exhibits longer IDT than the fuel-rich mixture. Here also, at 10 bar and $\phi = 1$ (Fig. 11a), all model overpredict the IDT below 625 K. For the lean condition at 15 bar (Fig. 11b) with CO_2 bath gas, all model underpredicts the IDT; however, the He model is closer to measurements compared to other two. Further, at 15 bar and rich conditions (Fig. 11c), our model prediction is better compared to He et al. and Cai et al. model.

The investigated temperature range is below the NTC area, which for OME_2 and OME_3 are in the temperature range of approx. 800–1000 K (same pressure and equivalence ratio, Fig. 12). Furthermore, literature data for OME_2 and OME_3 shown in Fig. 12 (temperature above 700 K, 20 bar) report that IDTs for $\phi = 1.0$ is the same.

Furthermore, comparing our present and previous experimental data presented in Fig. 10 and Fig. 11 (see also Fig. S12 in SM), we observe that OME_2 and OME_3 have similar IDT at $\phi = 1.0$ and 2.0 at pressure 10 and 15 bar, respectively. However, the IDT at $\phi = 0.5$ and 15 bar (Figs. 10c and 11b) is different for both fuels, which is expected; the IDT of OME_3 is almost twice as long as the IDT of OME_2 . The difference in IDT is mainly due to the different bath gas used. As mentioned above, for OME_3 ($\phi = 0.5$), we used CO_2 as bath gas. It is known that CO_2 has higher collider efficiency than N_2 , which mainly depends upon the structure of the species. For instance, in the present model, the collision efficiency of CO_2 is 1.5, while N_2 is 0.4. Therefore, using the different bath gas can significantly change the reaction velocity of reactions involving third body species (e.g., $\text{H}+\text{O}_2(\text{+M})=\text{HO}_2(\text{+M})$, M=third body), which eventually changes the system reactivity. Further, having different bath gas also alters the thermodynamic properties of the system. Overall, it can be observed in Figs. 10 and 11 that the proposed model in this work captures most of the experimental data nicely. The model accurately follows the observed trend in equivalence ratio and pressure. However, the model under-predicts the IDT of OME_2 and OME_3 at $\phi = 0.5$ by a factor of ~2.

Further, by comparing the IDT of OME_1 , OME_2 , and OME_3 using literature data (Fig. 12 and Figs. S12 and S13 in SM) in the temperature range 700–1200 K, we find that the IDT of OME_1 is longer than OME_2 . However, IDT of OME_2 and OME_3 are alike. Our previous work [17] showed that OME_1 exhibits a weak NTC behavior, which is also true for OME_2 and OME_3 (but not for OME_0). Furthermore, it can be observed in Fig. 12 for OME_1 (a) that the He model overpredicts the IDT at a temperature range ~700–950 K while the Ras model predicts shorter and longer IDT at high and low temperatures. For the Ras model, this is true for other conditions as well Fig. S14 ($\phi = 0.5-2.0$ and 10 bar). However, our model and Cai model both show good agreement with the experimental data. For OME_2 (b), all model follows the observed trend nicely and offers excellent predictions without significant discrepancies from each other. Similarly, for OME_3 (c), the He model over-predicts the IDTs in the NTC range, while our and Cai model can

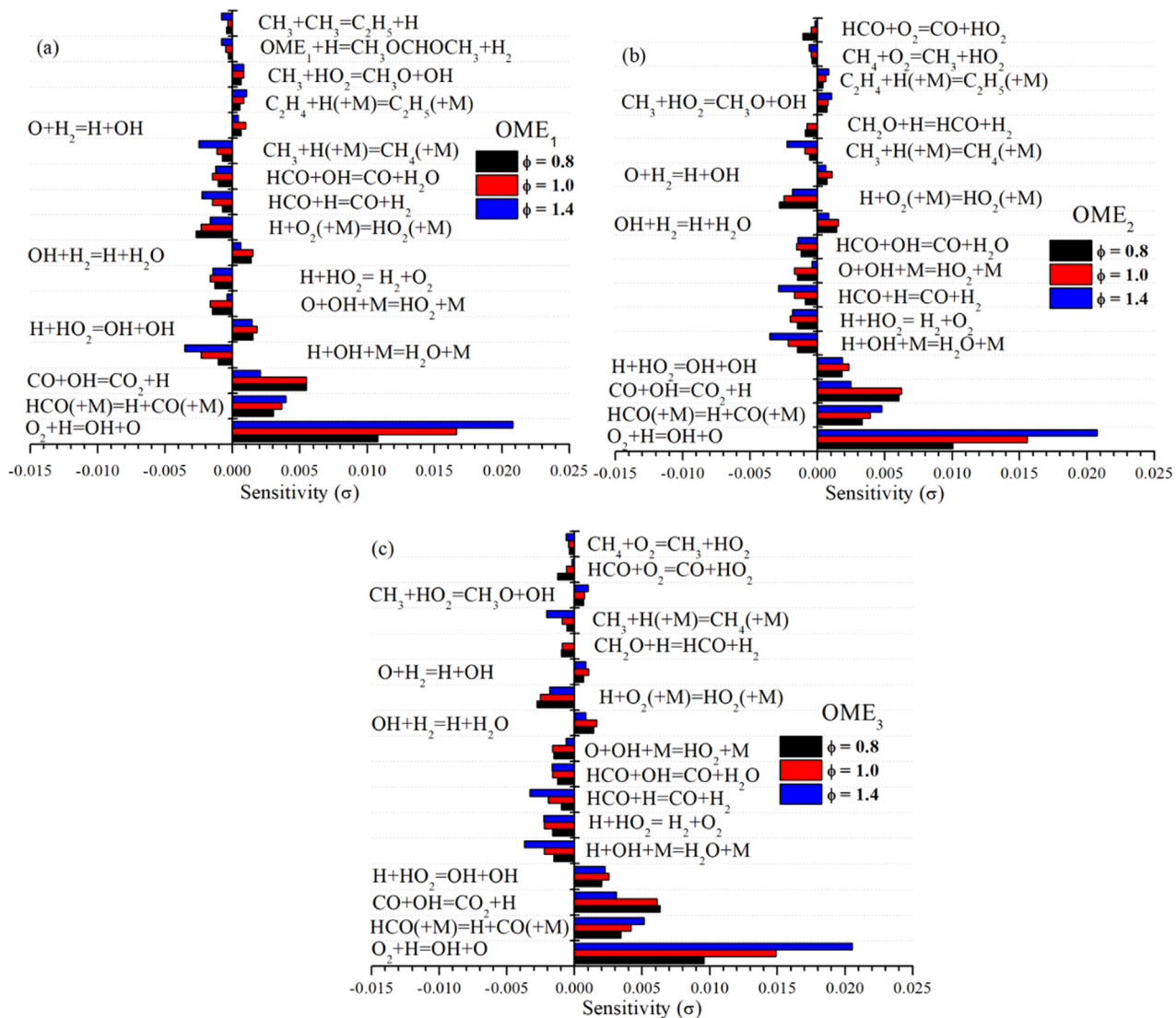


Fig. 9. Reactions sensitivity analysis towards laminar flame speed of OME₁/air (a), OME₂/air (b), OME₃/air (c) at $T_u = 443$ K, $P_u = 3$ bar and $\phi = 0.8, 1.0$ and 1.4 .

capture the whole range of experimental data very well. However, for $\phi = 1.0$ and 10 bar, as shown in Fig. S13 in supplementary material, our model outperforms both the He and Cai model. Further model validation and comparison with other literature models for OME₁, OME₂, and OME₃ for a wide range of conditions are demonstrated in the supplementary material (Figs. S12–S18). Comparing the results shown in Figs. 10, 11, and 12 and in the supplementary material, Figs. S12–S18 we can conclude that the present model is superior compared to Cai, He, and Ras model for IDT prediction.

We further note here that we do not want to optimize the model to predict the IDTs only. The main aim of the present work is to provide a kinetic model that is validated over a broad range of conditions rather than focusing on specific conditions. However, the discrepancies between the model predictions and experiments at low-temperature do call the need for future work on the chemistry of these fuels (OME₂ and OME₃).

4.5. Kinetic analysis at low temperature

Figure 13 shows the integrated mass flux analysis based on C-atom for OME₁ (a), OME₂ (b), and OME₃ (c) at 780 K, 20 bar, and $\phi = 1.0$ (only major paths are shown) using the present model. The

blue lines highlight the major O₂ addition pathways. The initial decomposition stage of OME_n ($n = 1-3$) follows the same behavior as shown in Fig. 8. At low-temperature, the H-abstraction from the fuel is primarily by OH radical rather than H-atom, as seen at flame conditions (Fig. 8). The kinetic analysis suggests that OME₁ (Fig. 13a) undergoes H-atom abstraction by OH, H, and HO₂ to yield primary fuel radical at α (44%, OME1B) and β (51%, OME1A) sites. Unlike high temperature, OH contributes the most and least is contributed by HO₂ radical. Furthermore, OME1A primarily undergoes a unimolecular dissociation path to yield CH₃OCH₂ (48%) and CH₂O (24%). The formed CH₃OCH₂ further decomposes to yield CH₃ and CH₂O. However, only 26% of OME1A undergoes O₂ addition which eventually leads to ketohydroperoxide (KET) and OH radicals. Interestingly for OME1B, O₂ addition is not happening at all. The formed OME1B exclusively undergoes unimolecular dissociation to yield CH₃OCHO and CH₃.

During OME₂ oxidation (Fig. 13b) formation of primary fuel radical at the α site (63%, OME2B) is favored compared to the β site (33%, OME2A), which contradicts OME₁ (Fig. 13a). The OME2A mainly undergoes unimolecular dissociation yielding OME1A (67%) and CH₂O (23%, not shown here). The small fraction of OME1A undergoes recombination with O₂ (9%, OME2AO₂). Here also, O₂ addition to radical at β site (OME2A) is favored while the radical at

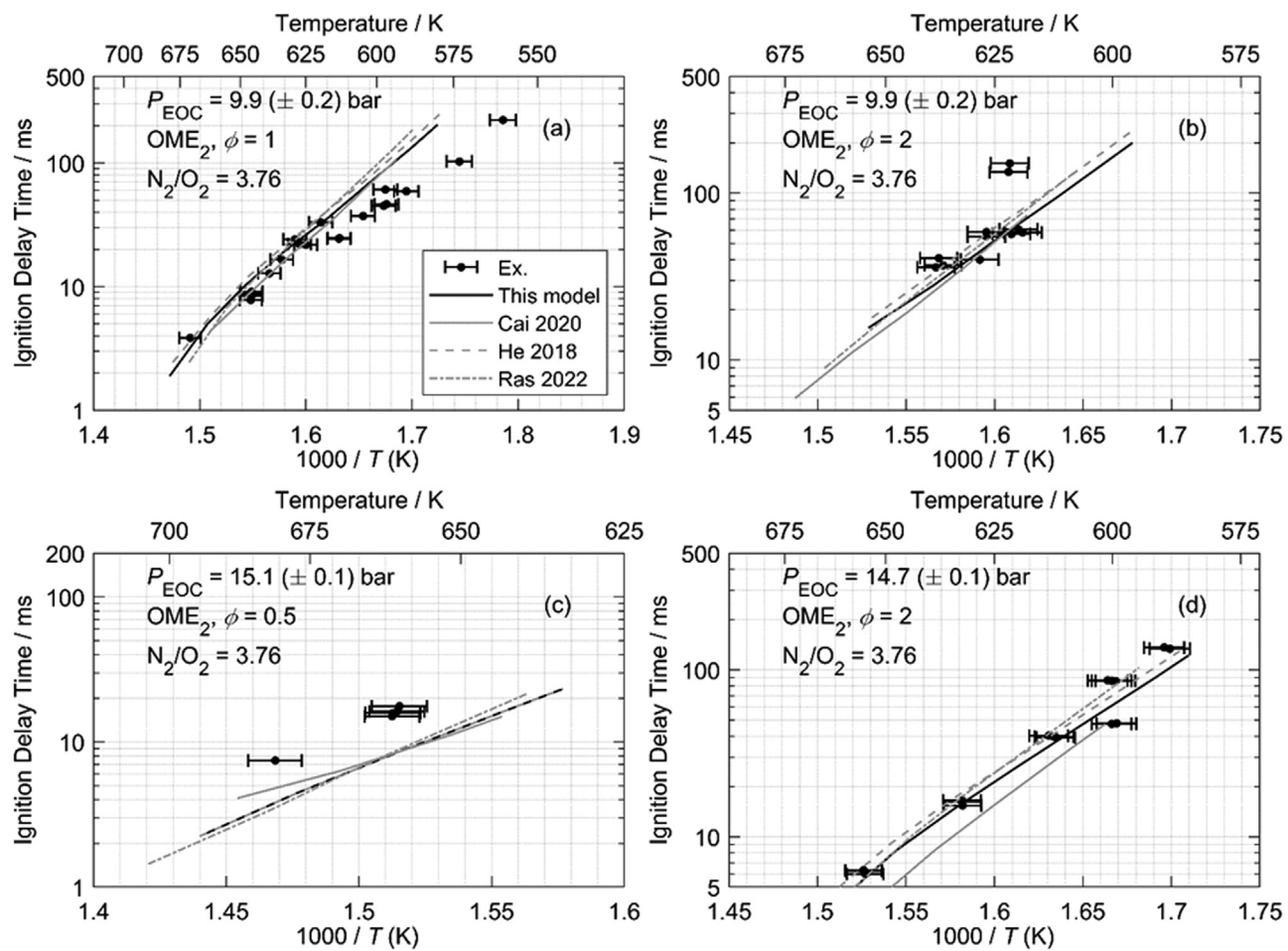


Fig. 10. Ignition delay times of OME_2/air . Symbols: measurement; (a) $\phi = 1.0$ and 10 bar from [24], (b) $\phi = 2.0$ and 10 bar (present work), (c) $\phi = 0.5$ and 15 bar (present work), (d) $\phi = 2.0$ and 15 bar (present work). Lines: model predictions; black solid lines: this work, grey solid lines: Cai et al. [10], grey dashed: He et al. [9], and dash-dotted: Ras et al. [25].

α site (OME_2B) mainly undergoes unimolecular dissociation yielding CH_3OCH_2 (primary fuel radical of OME_0) and CH_3OCHO . However, only 9% of OME_2A undergoes an O_2 addition path compared to OME_1A (26%, Fig. 13a) during OME_1 oxidation, which eventually leads to respective KET and OH formation. Further, the formed OME_1A follows a similar decomposition path as shown in Fig. 13a. In the case of OME_2 (Fig. 13b), there are two main O_2 addition pathways: one is with OME_2A , and the other is with one chain length shorter primary fuel radical (i.e., OME_1A), which leads to the formation of KET and OH. The additional OH formation pathway for OME_2 at lower temperatures explains the shorter ignition delay time than OME_1 , as observed in Fig. 12.

OME_3 (Fig. 13c) also undergoes H-atom abstraction by radicals OH, H, HO_2 , and CH_3 from α (24%, OME_3C), β (46%, OME_3B), and γ (25%, OME_3A) sites. The most favored path is the formation of OME_3B . As observed for OME_2 , here also O_2 addition path is most favored to the radical at terminal carbon atom OME_3A (8%) compared to OME_3B (1%, not shown here) and OME_3C (1%, not shown here). OME_3A mainly undergoes unimolecular dissociation to yield OME_2A and CH_2O . The formed OME_2A further undergoes unimolecular dissociation to yield OME_1A . The formed OME_2B directly forms OME_1A and CH_3OCHO (not shown here) via the unimolecular dissociation channel. For OME_2 and OME_3 , the O_2 addition to the primary fuel radical (at terminal carbon atom) is not preferred as compared to OME_1 (26% vs. 9% and 8%); instead, unimolecular dissociation paths are more favored (46% vs. 67% and 73%). Comparing the flux analysis for OME_2 (Fig. 13b) and OME_3

(Fig. 13c), we observe one more major pathway for O_2 addition (shown by blue lines), which all leads to the respective KET and OH radicals. Despite having an additional path for OH formation at low temperature, the IDT of OME_3 is not much different from OME_2 (Fig. 12). This can be explained by 1) the three primary fuel radicals formation during OME_3 oxidation compared to two primary fuel radicals of OME_2 and 2) the decrease in the flux towards the formation of the primary fuel radical, which favors O_2 addition, which is γ site (25%, OME_3A) for OME_3 and β site (33%, OME_2A) for OME_2 .

To generalize, OME_1 decomposes to its primary fuel radical (at α and β site). The formed radical further decomposes to yield primary fuel radical of OME_0 . OME_2 undergoes H-abstraction at α and β sites, leading to OME_1 and OME_0 primary fuel radicals. Similarly, decomposition of OME_3 leads to primary fuel radical of OME_2 , OME_1 , and OME_0 at an early stage. The O_2 addition channel mainly favors the primary fuel radical of OME_3 , OME_2 , OME_1 , and OME_0 at the terminal carbon atom, i.e., OME_3A , OME_2A , OME_1A , and CH_3OCH_2 . At low-temperature and high-pressure conditions, we also observe that OME_0 chemistry plays a significant role in the combustion behavior of higher chain length OMEs. The findings of our analysis are supported by the recent flow reactor experimental study of OME_n ($n = 0-5$) from Gaiser et al. [26]. They observed that the species pool during the oxidation of OME_n ($n = 0-5$) is nearly independent of the chain length of the OME_n . The primary decomposition channels of investigated OMEs are the same as observed in the flame condition where the primary fuel radical of

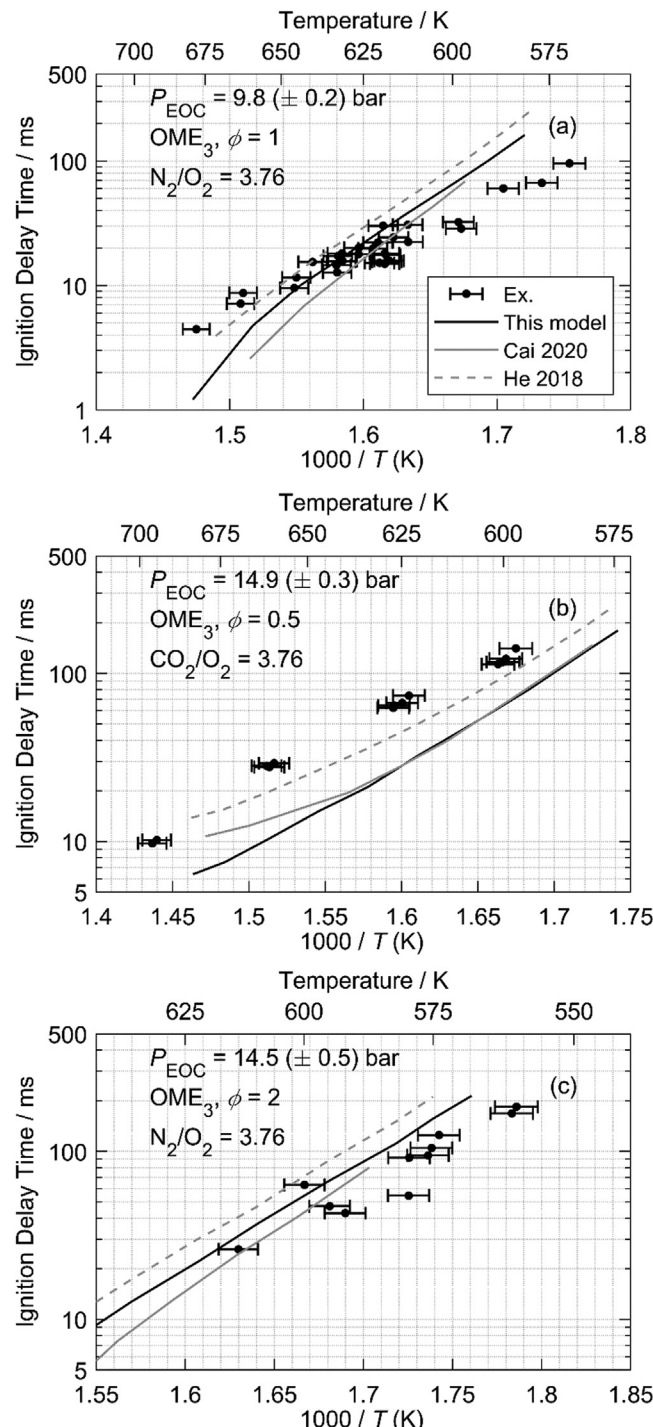
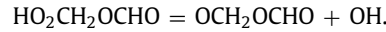
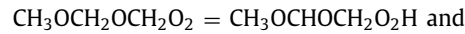
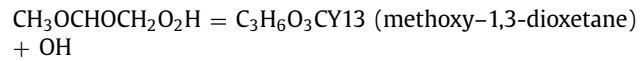


Fig. 11. Ignition delay times of OME_3 . Symbols: measurement, (a) $\phi = 1.0$ and 10 bar from [24] with air; (b) $\text{OME}_3/\text{O}_2/\text{CO}_2$ ($\phi = 0.5$, present work), (c) OME_3/air ($\phi = 2.0$, present work). Lines: model predictions; black solid lines: this work, grey solid lines: Cai et al. [10], and grey dashed: He et al. [9].

higher chain length OME yields the primary fuel radical of one chain length shorter OME, i.e., $\text{OME}_n > \text{OME}_{n-1} > \text{OME}_{n-2}$.

Figure 14 shows the reaction sensitivity analysis toward ignition delay time for OME_1 (a), OME_2 (b), and OME_3 (c) at 780 K, 20 bar, and $\phi = 1.0$. Positive sensitivity implies that the reaction increases the system reactivity (shortens the IDT) and vice versa. In line with the reaction flux analysis (Fig. 13), the topmost sensitive reaction for all OMEs is the H abstraction reaction from fuel by OH and HO_2 . The chain branching reaction $\text{H}_2\text{O}_2(+\text{M}) = \text{OH} + \text{OH}(+\text{M})$

and terminating reactions $\text{HO}_2 + \text{HO}_2 = \text{H}_2\text{O}_2 + \text{O}_2$ show positive and negative sensitivity, as expected for all OMEs. Furthermore, it is interesting to observe that for OME_2 and OME_3 reactions stemming from OME_1 and OME_0 chemistry are also among the most sensitive reactions i.e.



In line with the above flux analysis, this observation further suggests that the chemistry of smaller OMEs is crucial for accurately characterizing the combustion behavior of higher chain length OMEs. Further model validation against IDT of OME_1 , OME_2 , and OME_3 can be found in the supplementary material (Figs. S12–S18).

5. Model validation against experimental literature data

As mentioned earlier, the proposed kinetic model is extensively validated against the available literature data for OME_1 , OME_2 , and OME_3 . This work thus represents an extension of our previous work on DME and DMM [17]. For completeness, the results of our model validation against the literature data from jet-stirred and flow reactors for OME_2 and OME_3 are shown below. Model validation against speciation in the burner-stabilized flames can be found in the supplementary material (Figs. S31–S33). Since OME_0 and OME_1 were investigated in our previous study [17], model validation for them is shown in the supplementary material to demonstrate model predictive capability.

5.1. Speciation in a flow reactor

Figure 15 shows the species evolution as a function of temperature during $\text{OME}_2/\text{O}_2/\text{Ar}$ oxidation in a flow reactor at $\phi = 1.2$ and 1 atm. These experimental species profiles (symbols) are taken from Gaiser et al. [26]. Along with our model predictions, model performance from the literature is also shown for comparison. Solid lines show our model prediction, dashed lines show Cai et al. [10], and dotted lines show prediction using Ras et al. [25] model. It should be noted that the Ras model was developed targeting only OME_2 . The model from this work and Ras shows similar predictions for all species and follows the experimental trend well for the range of investigated temperatures. It also reasonably captures most of the experimental data. Further, it can be observed in Fig. 15a that the Cai model predicts the onset of fuel oxidation at 150 K higher than observed in the experiment. The present and Ras models nicely predict the onset of fuel decomposition. However, both model (present and Ras) underpredicts the fuel consumption at the temperature range 850 – 950 K. All model reproduces O_2 (d) and H_2O (h) reasonably well. Furthermore, it can be observed that the models reasonably capture CO (g) formation at a temperature above 1000 K but overpredicts CO_2 (b). High scatter on the data points for H_2 (e) and C_2H_6 (f) is observed in the experiment, and model predictions are reasonably good. Compared to other intermediate species model predictions of CH_2O (i) is quite different. The predicted maximum concentration of CH_2O by the present and Ras model is the same and is a factor ~ 2.5 higher compared to the experiment. However, the maximum concentration predicted by Cai model is closer to the experiment. It should also be noted that Cai model shows a clear offset on temperature as seen for fuel (a) indicating that initial fuel decomposition reactions in Cai model may not be properly characterized (as shown

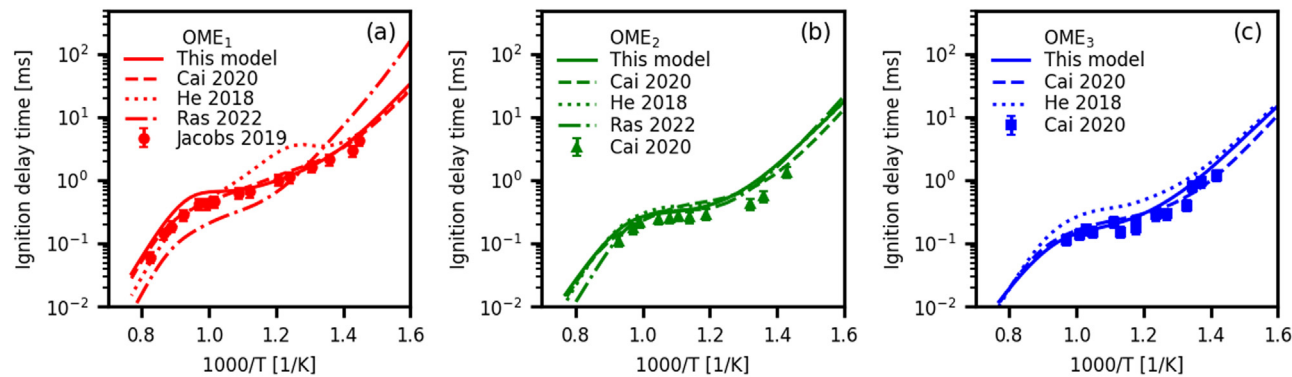


Fig. 12. Ignition delay time of OME₁/air (a), OME₂/air (b), and OME₃/air (c) at 20 bar, $\phi = 1.0$. Symbols: shock tube experiments from Jacobs et al. [54] (OME₁) and Cai et al. [10] (OME₂ and OME₃). Lines model predictions; solid lines: this model, dashed lines: Cai et al. [10], dotted: He et al. [9], and dash-dotted lines: Ras et al. [25].

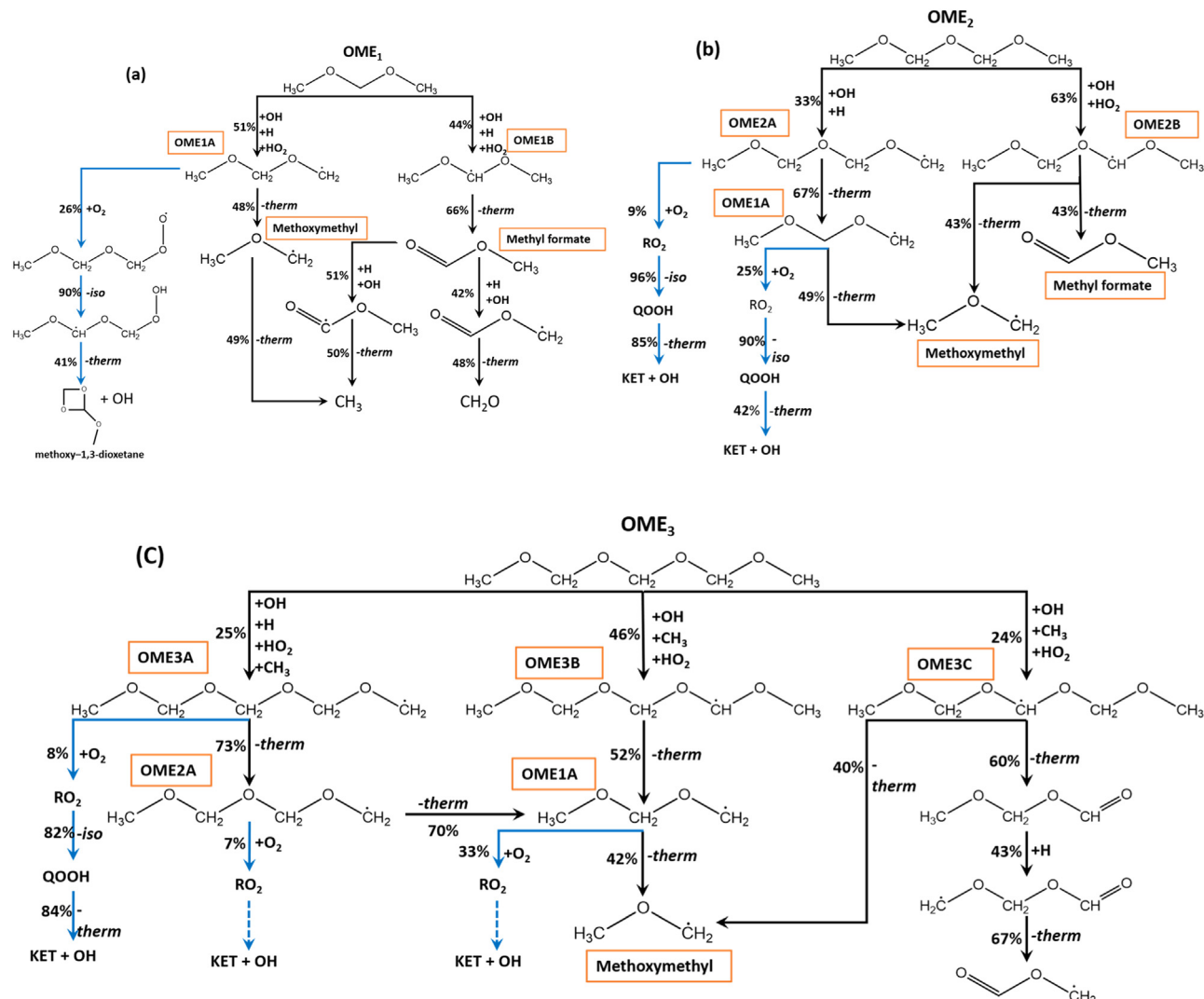


Fig. 13. Integrated mass flux analysis based on C-atom at 780 K, 20 bar, and $\phi = 1.0$ at complete fuel consumption using the present model.

in Fig. 2). Overall, Cai model is the optimized model targeted for auto-ignition of fuels OME₂, OME₃, and OME₄.

We further note that these experimental data for OME₂ are the first to be reported in the literature at flow reactor conditions; therefore, the comparison with other reactor data is not possible (e.g., no oxidation data available for jet-stirred reactor). Furthermore, the authors in their work [26] stated that the statistical and

relative uncertainty of the instrument is below 10%. For species using direct calibration, uncertainty ranges between 15 and 20%, while for non-calibrated species, the uncertainty can increase to a factor of 2–4. The species for direct calibration includes only major species. More experimental data at similar and different conditions from various experimental setups is warranted for validation and robust kinetic model development.

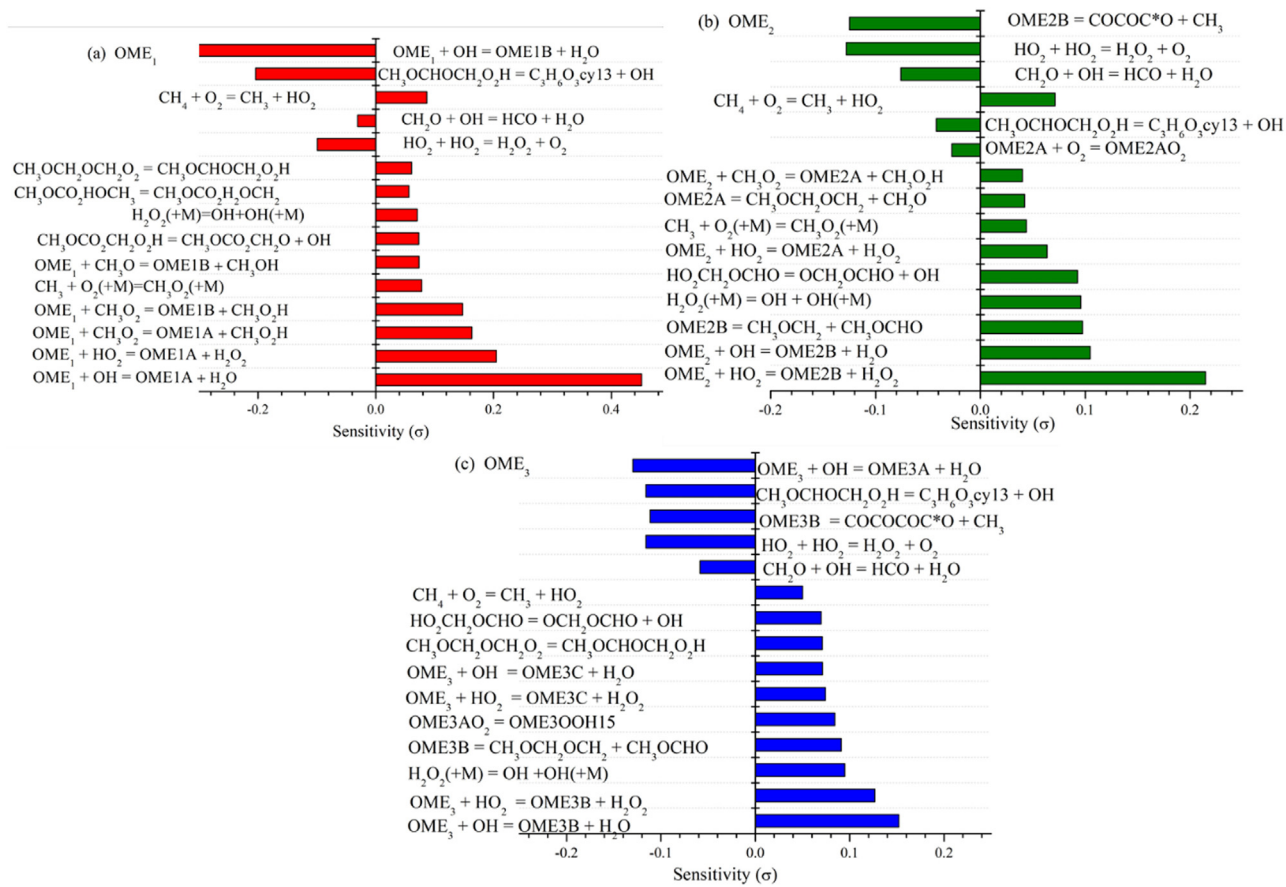


Fig. 14. Brute force reaction sensitivity analysis towards ignition delay time at 780 K, 20 bar, and $\phi = 1.0$. OME₁/air (a), OME₂/air (b) and OME₃/air (c) with present model.

5.2. Speciation in a jet-stirred reactor

Figure 16 shows the evolution of species as a function of temperature during the oxidation of OME₃/O₂/N₂ in a jet-stirred reactor at $\phi = 1.0$ and 1 atm. Experimental species profiles (symbols) are from Qiu et al. [11]. Together with our model predictions (solid lines), comparisons with Cai et al. [10] (dashed lines) and He et al. [9] (dotted lines) are also shown. It can be observed in Fig. 16a that our model captures the fuel consumption profile very well. The He model predicts the onset of fuel consumption at lower temperatures, showing higher reactivity. However, the Cai model slightly overpredicts fuel above 750 K. Further, the discrepancies between the model predictions for major species O₂ (d), CO (g), and CO₂ (b) are not significant. However, O₂ is overpredicted at temperatures above 850 K. For H₂ (e), the He model shows over predictions at higher temperatures. Similar observations can be made for species CH₄ (h), C₂H₄ (c), and C₂H₆ (f). Furthermore, special attention is paid to CH₃OH (i), for which the He and our model significantly underpredict the concentration. The Cai model shows better prediction but can not still capture the experimental data. The CH₃OH profile is unique because it exhibits two peaks while other species do not. Interestingly all of the models follow this observed trend.

We showed that none of the kinetic models could accurately predict the CH₃OH profile while reasonably capturing most of the other species. To understand this disparity, we conducted a sensitivity analysis of the critical reactions that influence CH₃OH profile. Fig. 17 displays the 25 most sensitive reactions influencing CH₃OH at 660 K (near the first peak). Note that a reaction with a positive sensitivity coefficient enhances the concentration of the species and vice versa. It can be observed that most of the reactions stem from the OME and less from the base chemistry

(H₂/O₂/C₁). It is known that reactions from OME sub-mechanism have higher uncertainty. The rate parameters of the reactions in base chemistry are well established in the literature. Further, it should be noted that our base mechanism has been extensively validated in our earlier work [17,41,42,45]. Therefore, in this analysis, we only deal with the reactions from OME chemistry displayed in Fig. 17.

We analyzed three different cases: (i) rate parameters of the reactions with positive sensitivity were increased by 50%; (ii) rate parameters of the reactions with negative sensitivity were decreased by 50%, and (iii) rate parameters for all the reactions were simultaneously changed (applying case (i) and (ii) together). The results of these analyses are displayed in Fig. S19 in the supplementary material. As expected, the first case (solid blue lines) and the second case (dashed blue lines) brings the model predictions closer to the experimental data; however, the impact of reaction exhibiting positive sensitivity is higher compared to reactions showing negative sensitivity. For the third case (solid green line), the model prediction is improved compared to the first two cases, particularly at low temperatures. However, the model predictive capability for the first and third cases deteriorates the fuel profile in the NTC region (see Fig. S19a in SM). From the above analysis, we may conclude that the observed discrepancy in CH₃OH prediction does not stem from the rate parameters of the most sensitive reactions towards CH₃OH only.

Furthermore, the direct CH₃OH formation path during fuel oxidation is the reaction of CH₃O with OME₃ (see Section 3). Neither theoretical nor experimental study has yet been reported in the literature for this reaction. As mentioned above, in this work, the rate constant of this reaction is adopted from Cai et al. [10], who estimated the rate constant based on the reaction class analogy of

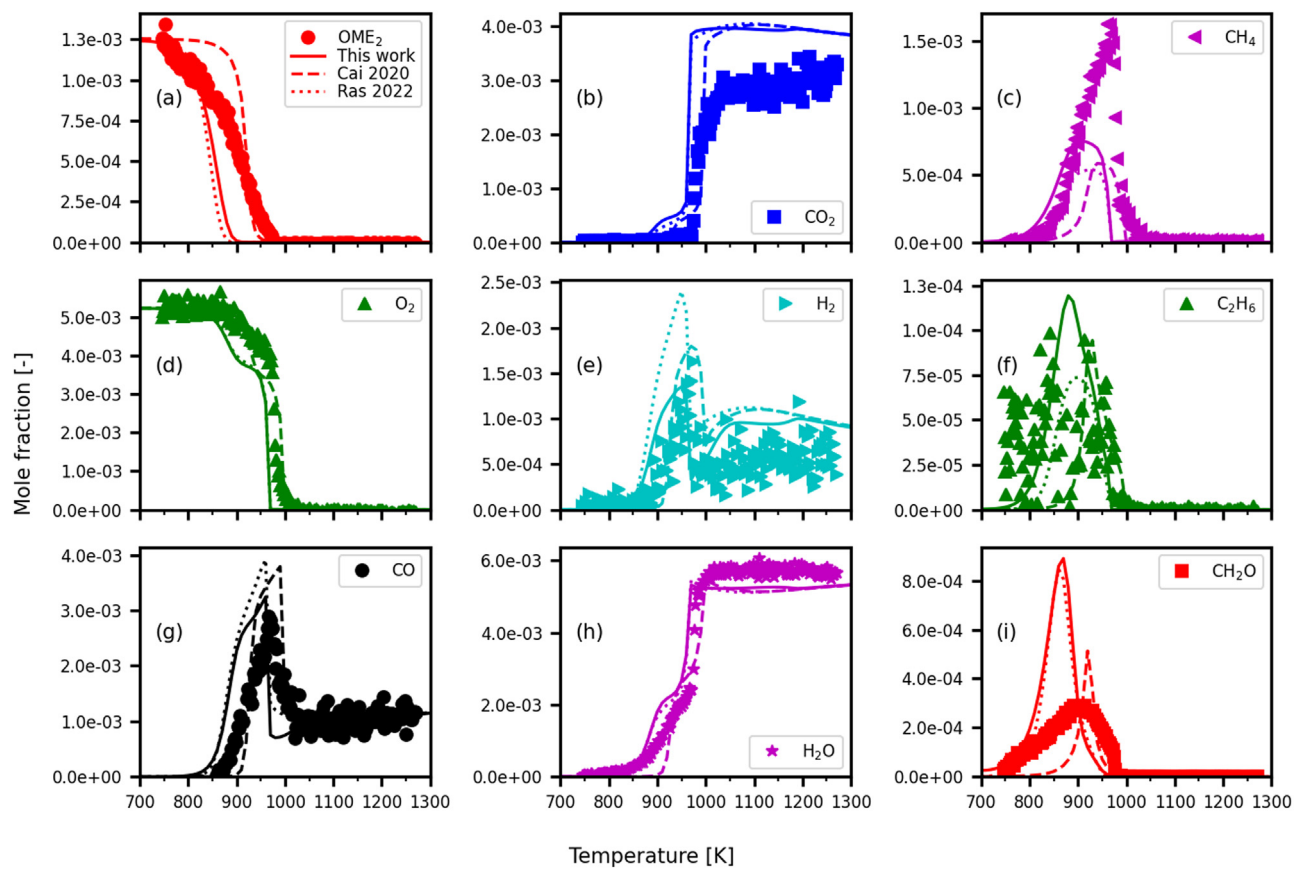


Fig. 15. Oxidation of OME₂/O₂/Ar in a flow reactor at $\phi = 1.2$, 1 atm and $\tau = 1.7 - 2.8$ s. Symbols experimental data from Gaiser et al. [26], solid lines: model predictions from this work, dashed lines: Cai et al. [10] model, and dotted lines: Ras et al. [25] model.

small molecules. However, recently Ras et al. [25] theoretically determined the rate constant of OME₂ + CH₃O reaction using a high level of quantum chemical study. This is the closest analogy that one can use for the OME₃ + CH₃O reaction. For the investigation, we used the rate constant of Ras et al. [25] for H abstraction by CH₃O from OME₃. The impact on model prediction is shown in Fig. S23 in SM. It can be observed that the influence on CH₃OH or any other species is insignificant.

Likewise, H abstraction by CH₃ from OME₃ is the direct CH₄ formation route. The rate constant in this study is adopted from the modeling work of He et al. [9], who estimated based on the analogy with DME and diethyl ether (DEE). The reaction rate of OME₂ + CH₃ is theoretically calculated by Ras et al. [25], which is the closest analogy one can make for OME₃ + CH₃. As shown in Fig. 16, the present model predicts the maximum mole fraction of CH₄ by a factor of 1.7. Implementing the rate constant of Ras et al. [25] with analogy improved the model prediction. However, the predicted maximum mole fraction of CH₄ is still higher by a factor of 1.3 compared to the measured value. This does not still explain the discrepancies between model prediction and measurements. Further, we found that implementing the Ras et al. [25] rate parameter in our model deteriorates the prediction for ignition delay time. The above analysis clearly suggests that more investigation is needed in the future to describe these discrepancies, which are beyond the scope of this study.

Further, it should be noted that these data sets (Fig. 16) are the first to be reported in the literature in jet-stirred reactor conditions. Therefore, a further experiment is highly desirable for future model improvement and development. Overall the proposed kinetic model can perform reasonably well over a wide range of investigated conditions (Table 2). Additional model validation against

the flow and jet-stirred reactor experiments can be found in the supplementary material (Figs. S20–S30).

6. Conclusions

Laminar flame speeds and Markstein length of OME₁, OME₂, and OME₃ at $T_u = 393$ K and 443 K, $P_u = 1, 3$, and 5 bar, and equivalence ratios between 0.8 and 1.6 are experimentally studied using the constant volume chamber. The ignition delay time of OME₂ and OME₃ are measured using an RCM at a pressure of $P_u = 10$ and 15 bar, equivalence ratios of 0.5–2.0, and a temperature range of $T_u = 550$ to 680 K. Based on the present measurements and published experimental data, a detailed reaction mechanism for the pyrolysis and oxidation of OME₁, OME₂, and OME₃ has been developed. Several published experiments have been selected to demonstrate that essential features of these OMEs chemistry are well captured by the here derived and broadly validated reaction mechanism. Overall, there is a good agreement between model predictions and experimental measurements for a wide range of conditions. Comparing the LFS of OME₀, OME₁, OME₂, and OME₃ from our previous and this work, we found that OME_n ($n = 0-3$) have a similar laminar flame speed regardless of their chain length. The model reveals that the decomposition of higher chain length OME_n in the initial phase quickly yields the primary fuel radical of OME_{n-1} and OME_{n-2}. The further decomposition of OME_{n-1} primary fuel radical yields OME_{n-2} primary fuel radical, which predominately leads to the chemistry of OME₀ and CH₃OCHO.

In the investigated temperature range, the ignition delay time of OME₂ and OME₃ was the same when the same diluent (N₂) was used for $\phi = 1$ and 2. However, at $\phi = 0.5$, changing the diluent from N₂ to CO₂ prolonged the ignition delay time. OME_n ($n = 1-3$)

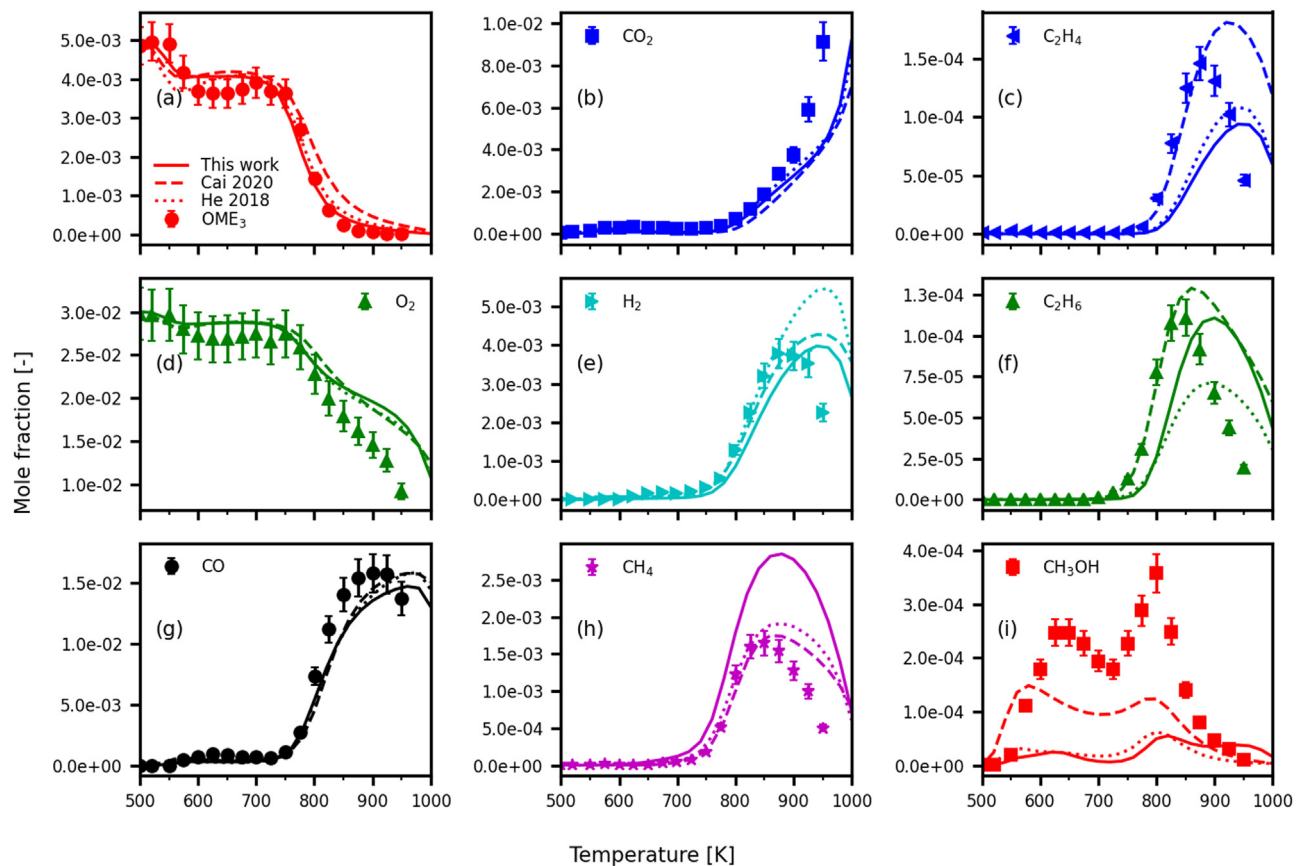


Fig. 16. Oxidation of $\text{OME}_3/\text{O}_2/\text{N}_2$ in a jet-stirred reactor at $\phi = 1.0$, 1 atm and $\tau = 2$ s. Symbols experimental data from Qiu et al. [11], solid lines: model predictions from this work, dashed lines: Cai et al. [10] model predictions, and dotted lines: He et al. [9] model.

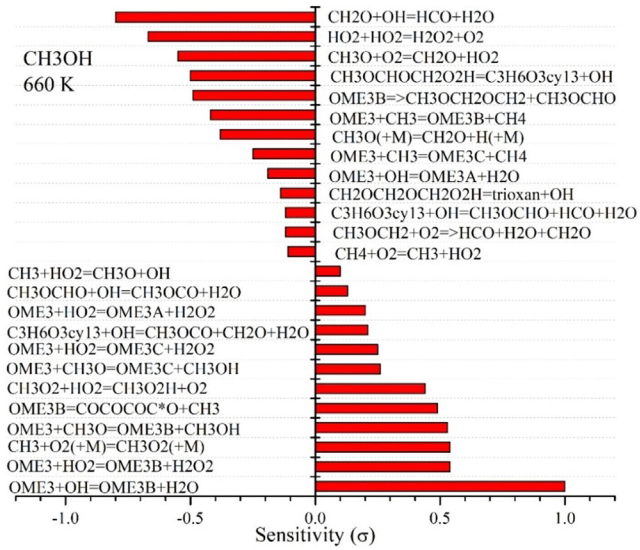


Fig. 17. Reaction sensitivity analysis towards CH_3OH at 660 K for the conditions given in Fig. 16.

3) exhibits weak NTC behavior compared to OME_0 (i.e., DME). The model reveals that at low temperatures as well, unimolecular dissociation channels of primary fuel radicals of OME_n ($n = 1-3$) are most favored. In contrast, the O_2 addition path is the least favored. The O_2 addition to the primary fuel radical at the terminal carbon atom (β site for OME_1 and OME_2 and γ for OME_3) is the

preferred one compared to radical at other carbon sites. While for OME_0 , the recombination of O_2 to the primary fuel radical is the most favored, and the least favored is the unimolecular dissociation path. This explains the weak NTC regime of OME_n ($n = 1-3$) compared to OME_0 . The model reveals that the chemistry of short-chain length OME (i.e., OME_0 and OME_1) is crucial for characterizing the oxidation behavior of longer chain length OME.

The developed model in this work is validated over a wide range of experimental conditions, which includes: laminar flame speed, ignition delay time, speciation in jet-stirred and flow reactor, as well as burner stabilized flame for OME_0 , OME_1 , OME_2 , and OME_3 . The present model slightly underpredicts the laminar flame speed of OME_2 and OME_3 at 3 and 5 bar and $\phi = 0.9 - 1.2$. The model predicted ignition delay time for a wide range of conditions are fairly in good agreement with the experimental data for OME_1 , OME_2 , and OME_3 . However, the model unpredicts the present experimental data for OME_2 and OME_3 , particularly under lean conditions ($\phi = 0.5$). The developed model also performs well in reproducing the experimental speciation data of flow and jet-stirred reactor.

Furthermore, the performance of the kinetic model developed in this work is compared against the available literature models. The mechanism developed in this work can be used as a base mechanism for developing a kinetic model for OME_n ($n > 3$). However, more experimental data from different setups and a wide range of conditions for OME_n ($n > 1$) is needed to validate further and develop a robust model. In addition, theoretical quantum study is highly desired for the accurate rate parameters characterization of the reactions as well as establishing a new reaction pathway if exist to build a robust kinetic model.

Declaration of Competing Interest

The authors declare that they have no known competing financial interests or personal relationships that could have appeared to influence the work reported in this paper.

Acknowledgments

Financial support by the Deutsche Forschungsgemeinschaft within the framework of the DFG research group FOR 1993 "Multi-functional conversion of chemical species and energy" (229243862) is gratefully acknowledged. The authors from KIT like to thank N. Schmitz (TU Kaiserslautern) and J. Burger (TU Munich) for providing the OME-fuels and the support of OME Technologies (Kaiserslautern) and WDG Solvent (Wittenberge), INEOS Paraform (Mainz).

Supplementary materials

Supplementary material associated with this article can be found, in the online version, at doi:[10.1016/j.combustflame.2022.112426](https://doi.org/10.1016/j.combustflame.2022.112426).

References

- [1] M. Ouda, G. Yarce, R.J. White, M. Hadrich, D. Himmel, A. Schaadt, H. Klein, E. Jacob, I. Krossing, Poly(oxymethylene) dimethyl ether synthesis – a combined chemical equilibrium investigation towards an increasingly efficient and potentially sustainable synthetic route, *React. Chem. Eng.* 2 (2017) 50–59, doi:[10.1039/C6RE00145A](https://doi.org/10.1039/C6RE00145A).
- [2] L. Lautenschütz, D. Oestreich, P. Haltenort, U. Arnold, E. Dinjus, J. Sauer, Efficient synthesis of oxymethylene dimethyl ethers (OME) from dimethoxymethane and trioxane over zeolites, *Fuel Process. Technol.* 165 (2017) 27–33, doi:[10.1016/j.fuproc.2017.05.005](https://doi.org/10.1016/j.fuproc.2017.05.005).
- [3] H. Liu, Z. Wang, Y. Li, Y. Zheng, T. He, J. Wang, Recent progress in the application in compression ignition engines and the synthesis technologies of polyoxymethylene dimethyl ethers, *Appl. Energy* 233–234 (2019) 599–611, doi:[10.1016/j.apenergy.2018.10.064](https://doi.org/10.1016/j.apenergy.2018.10.064).
- [4] K.D. Vertin, J.M. Ohi, D.W. Naegeli, K.H. Childress, G.P. Hagen, C.I. McCarthy, A.S. Cheng, R.W. Dibble, Methylal and methylal-diesel blended fuels for use in compression-ignition engines, in: SAE Tech. Pap., 1999: pp. 1999-01-1508. doi:[10.4271/1999-01-1508](https://doi.org/10.4271/1999-01-1508).
- [5] O.I. Awad, X. Ma, M. Kamil, O.M. Ali, Y. Ma, S. Shuai, Overview of polyoxymethylene dimethyl ether additive as an eco-friendly fuel for an internal combustion engine: Current application and environmental impacts, *Sci. Total Environ.* 715 (2020) 136849, doi:[10.1016/j.scitotenv.2020.136849](https://doi.org/10.1016/j.scitotenv.2020.136849).
- [6] P. Dworschak, V. Berger, M. Härtl, G. Wachtmeister, Neat Oxymethylene ethers: combustion performance and emissions of OME₂, OME₃, OME₄ and OME₅ in a single-cylinder diesel engine, *SAE Tech. Pap.* 2020-April (2020). doi:[10.4271/2020-01-0805](https://doi.org/10.4271/2020-01-0805).
- [7] N. Li, W. Sun, S. Liu, X. Qin, Y. Zhao, Y. Wei, Y. Zhang, A comprehensive experimental and kinetic modeling study of dimethoxymethane combustion, *Combust. Flame* 233 (2021) 111583, doi:[10.1016/j.combustflame.2021.111583](https://doi.org/10.1016/j.combustflame.2021.111583).
- [8] S. Eckart, C. Fritzsche, C. Krasselt, H. Krause, Determining the laminar burning velocity of nitrogen diluted dimethoxymethane (OME₁) using the heat-flux burner method: Numerical and experimental investigations, *Int. J. Energy Res.* 45 (2021) 2824–2836, doi:[10.1002/er.5978](https://doi.org/10.1002/er.5978).
- [9] T. He, Z. Wang, X. You, H. Liu, Y. Wang, X. Li, X. He, A chemical kinetic mechanism for the low- and intermediate-temperature combustion of Polyoxymethylene Dimethyl Ether 3 (PODE₃), *Fuel* 212 (2018) 223–235, doi:[10.1016/j.fuel.2017.09.080](https://doi.org/10.1016/j.fuel.2017.09.080).
- [10] L. Cai, S. Jacobs, R. Langer, F. vom Lehn, K.A. Heufer, H. Pitsch, Auto-ignition of oxymethylene ethers (OME_n, n=2–4) as promising synthetic e-fuels from renewable electricity: shock tube experiments and automatic mechanism generation, *Fuel* 264 (2020) 116711, doi:[10.1016/j.fuel.2019.116711](https://doi.org/10.1016/j.fuel.2019.116711).
- [11] Z. Qiu, A. Zhong, Z. Huang, D. Han, An experimental and modeling study on polyoxymethylene dimethyl ether 3 (PODE₃) oxidation in a jet stirred reactor, *Fundam. Res.* (2021), doi:[10.1016/j.fmre.2021.09.005](https://doi.org/10.1016/j.fmre.2021.09.005).
- [12] J.M. Ngugi, S. Richter, M. Braun-Unkhoff, C. Naumann, M. Köhler, U. Riedel, A study on fundamental combustion properties of oxymethylene ether-2, *J. Eng. Gas Turbines Power* 144 (2022) 011014–1, doi:[10.1115/1.4052097](https://doi.org/10.1115/1.4052097).
- [13] S. Ren, Z. Wang, B. Li, H. Liu, J. Wang, Development of a reduced polyoxymethylene dimethyl ethers (PODE_n) mechanism for engine applications, *Fuel* 238 (2019) 208–224, doi:[10.1016/j.fuel.2018.10.111](https://doi.org/10.1016/j.fuel.2018.10.111).
- [14] W. Sun, G. Wang, S. Li, R. Zhang, B. Yang, J. Yang, Y. Li, C.K. Westbrook, C.K. Law, Speciation and the laminar burning velocities of poly(oxymethylene) dimethyl ether 3 (POMDME₃) flames: an experimental and modeling study, *Proc. Combust. Inst.* 36 (2017) 1269–1278, doi:[10.1016/j.proci.2016.05.058](https://doi.org/10.1016/j.proci.2016.05.058).
- [15] S. Richter, T. Kathrotia, M. Braun-Unkhoff, C. Naumann, M. Köhler, Influence of oxymethylene ethers (OME_n) in mixtures with a diesel surrogate, *Energies* 14 (2021) 7848, doi:[10.3390/en142737848](https://doi.org/10.3390/en142737848).
- [16] J.M. Ngugi, S. Richter, M. Braun-Unkhoff, C. Naumann, U. Riedel, A study on fundamental combustion properties of oxymethylene ether-1, the primary reference fuel 90, and their blend: experiments and modeling, *Combust. Flame* (2022) 111996, doi:[10.1016/j.combustflame.2022.111996](https://doi.org/10.1016/j.combustflame.2022.111996).
- [17] K.P. Shrestha, S. Eckart, A.M. Elbaz, B.R. Giri, C. Fritzsche, L. Seidel, W.L. Roberts, H. Krause, F. Mauss, A comprehensive kinetic model for dimethyl ether and dimethoxymethane oxidation and NO_x interaction utilizing experimental laminar flame speed measurements at elevated pressure and temperature, *Combust. Flame* 218 (2020) 57–74, doi:[10.1016/j.combustflame.2020.04.016](https://doi.org/10.1016/j.combustflame.2020.04.016).
- [18] H. Liu, Z. Wang, J. Wang, X. He, Improvement of emission characteristics and thermal efficiency in diesel engines by fueling gasoline/diesel/PODE_n blends, *Energy* 97 (2016) 105–112, doi:[10.1016/j.energy.2015.12.110](https://doi.org/10.1016/j.energy.2015.12.110).
- [19] H. Kuszewski, Physical and chemical properties of 1-butanol-diesel fuel blends, *Energy Fuels* 32 (2018) 11619–11631, doi:[10.1021/acs.energyfuels.8b02912](https://doi.org/10.1021/acs.energyfuels.8b02912).
- [20] I.M. Sivebaek, J. Jakobsen, The viscosity of dimethyl ether, *Tribol. Int.* 40 (2007) 652–658, doi:[10.1016/j.triboint.2005.11.005](https://doi.org/10.1016/j.triboint.2005.11.005).
- [21] M.E. Tat, J.H. Van Gerpen, The kinematic viscosity of biodiesel and its blends with diesel fuel, *JAOCS, J. Am. Oil Chem. Soc.* 76 (1999) 1511–1513, doi:[10.1007/s11746-999-0194-0](https://doi.org/10.1007/s11746-999-0194-0).
- [22] J. Wu, Z. Xu, Z. Liu, B. Wang, Density and viscosity of saturated liquid dimethoxymethane from (218.15 to 383.15) K, *J. Chem. Eng. Data* 50 (2005) 966–968, doi:[10.1021/je049559v](https://doi.org/10.1021/je049559v).
- [23] S. Eckart, L. Cai, C. Fritzsche, F. vom Lehn, H. Pitsch, H. Krause, Laminar burning velocities, CO, and NO_x emissions of premixed polyoxymethylene dimethyl ether flames, *Fuel* 293 (2021) 120321, doi:[10.1016/j.fuel.2021.120321](https://doi.org/10.1016/j.fuel.2021.120321).
- [24] S. Drost, R. Schießl, M. Werler, J. Sommerer, U. Maas, Ignition delay times of polyoxymethylene dimethyl ether fuels (OME₂ and OME₃) and air: measurements in a rapid compression machine, *Fuel* 258 (2019) 116070, doi:[10.1016/j.fuel.2019.116070](https://doi.org/10.1016/j.fuel.2019.116070).
- [25] K. De Ras, M. Kusenberg, G. Vanhove, Y. Fenard, A. Eschenbacher, R.J. Varghese, J. Aerssens, R. Van de Vijver, L.S. Tran, J.W. Thybaut, K.M. Van Geem, A detailed experimental and kinetic modeling study on pyrolysis and oxidation of oxymethylene ether-2 (OME-2), *Combust. Flame* 238 (2022) 111914, doi:[10.1016/j.combustflame.2021.111914](https://doi.org/10.1016/j.combustflame.2021.111914).
- [26] N. Gaiser, T. Bierkandt, P. Oßwald, J. Zinsmeister, T. Kathrotia, S. Shaqiri, P. Hemberger, T. Kasper, M. Aigner, M. Köhler, Oxidation of oxymethylene ether (OME_{0–5}): an experimental systematic study by mass spectrometry and photoelectron photoion coincidence spectroscopy, *Fuel* 313 (2022) 122650, doi:[10.1016/j.fuel.2021.122650](https://doi.org/10.1016/j.fuel.2021.122650).
- [27] K. De Ras, M. Kusenberg, J.W. Thybaut, K.M. Van Geem, Unraveling the carbene chemistry of oxymethylene ethers: experimental investigation and kinetic modeling of the high-temperature pyrolysis of OME-2, *Proc. Combust. Inst.* (2022), doi:[10.1016/j.proci.2022.07.069](https://doi.org/10.1016/j.proci.2022.07.069).
- [28] N. Gaiser, H. Zhang, T. Bierkandt, S. Schmitt, J. Zinsmeister, T. Kathrotia, P. Hemberger, S. Shaqiri, T. Kasper, M. Aigner, P. Oßwald, M. Köhler, Investigation of the combustion chemistry in laminar, low-pressure oxymethylene ether flames (OME_{0–4}), *Combust. Flame* (2022) 112060, doi:[10.1016/j.combustflame.2022.112060](https://doi.org/10.1016/j.combustflame.2022.112060).
- [29] X. Zhong, H. Wang, Q. Zuo, Z. Zheng, J. Wang, W. Yin, M. Yao, Experimental and kinetic modeling studies of polyoxymethylene dimethyl ether (PODE) pyrolysis in jet stirred reactor, *J. Anal. Appl. Pyrolysis* 159 (2021) 105332, doi:[10.1016/j.jaat.2021.105332](https://doi.org/10.1016/j.jaat.2021.105332).
- [30] Q. Wang, W. Sun, L. Guo, S. Lin, P. Cheng, H. Zhang, Y. Yan, Experimental and kinetic study on the laminar burning speed, Markstein length and cellular instability of oxygenated fuels, *Fuel* 297 (2021) 120754, doi:[10.1016/j.fuel.2021.120754](https://doi.org/10.1016/j.fuel.2021.120754).
- [31] F. Rau, S. Hartl, S. Voss, M. Still, C. Hasse, D. Trimis, Laminar burning velocity measurements using the Heat Flux method and numerical predictions of iso-octane/ethanol blends for different preheat temperatures, *Fuel* 140 (2015) 10–16, doi:[10.1016/j.fuel.2014.09.059](https://doi.org/10.1016/j.fuel.2014.09.059).
- [32] S. Eckart, L. Pizzuti, C. Fritzsche, H. Krause, Experimental study and proposed power correlation for laminar burning velocity of hydrogen-diluted methane with respect to pressure and temperature variation, *Int. J. Hydrg. Energy* 47 (2022) 6334–6348, doi:[10.1016/j.ijhydene.2021.11.243](https://doi.org/10.1016/j.ijhydene.2021.11.243).
- [33] A.P. Kelley, C.K. Law, Nonlinear effects in the extraction of laminar flame speeds from expanding spherical flames, *Combust. Flame* 156 (2009) 1844–1851, doi:[10.1016/j.combustflame.2009.04.004](https://doi.org/10.1016/j.combustflame.2009.04.004).
- [34] Z. Chen, On the accuracy of laminar flame speeds measured from outwardly propagating spherical flames: methane/air at normal temperature and pressure, *Combust. Flame* 162 (2015) 2442–2453, doi:[10.1016/j.combustflame.2015.02.012](https://doi.org/10.1016/j.combustflame.2015.02.012).
- [35] A.A. Konnov, A. Mohammad, V.R. Kishore, N. Il Kim, C. Prathap, S. Kumar, A comprehensive review of measurements and data analysis of laminar burning velocities for various fuel-air mixtures, *Prog. Energy Combust. Sci.* 68 (2018) 197–267, doi:[10.1016/j.pecs.2018.05.003](https://doi.org/10.1016/j.pecs.2018.05.003).
- [36] W. Li, B. Mei, Y. Li, S. Eckart, H. Krause, S. Ma, Y. Zhang, Insight into fuel isomeric effects on laminar flame propagation of pentanones, *Proc. Combust. Inst.* 38 (2021) 2135–2142, doi:[10.1016/j.proci.2020.06.113](https://doi.org/10.1016/j.proci.2020.06.113).
- [37] S. Drost, M.S. Aznar, R. Schießl, M. Ebert, J.Y. Chen, U. Maas, Reduced reaction mechanism for natural gas combustion in novel power cycles, *Combust. Flame* 223 (2021) 486–494, doi:[10.1016/j.combustflame.2020.09.029](https://doi.org/10.1016/j.combustflame.2020.09.029).
- [38] S. Drost, D. Kaczmarek, S. Eckart, J. Herzler, R. Schießl, C. Fritzsche, M. Fikri, B. Atakan, T. Kasper, H. Krause, C. Schulz, U. Maas, Experimental investigation

- of ethanol oxidation and development of a reduced reaction mechanism for a wide temperature range, *Energy Fuels* 35 (2021) 14780–14792, doi:[10.1021/acs.energyfuels.1c01993](https://doi.org/10.1021/acs.energyfuels.1c01993).
- [39] C.J. Sung, H.J. Curran, Using rapid compression machines for chemical kinetics studies, *Prog. Energy Combust. Sci.* 44 (2014) 1–18, doi:[10.1016/j.pecs.2014.04.001](https://doi.org/10.1016/j.pecs.2014.04.001).
- [40] U. Burke, K.P. Somers, P. O'Toole, C.M. Zinner, N. Marquet, G. Bourque, E.L. Petersen, W.K. Metcalfe, Z. Serinyel, H.J. Curran, An ignition delay and kinetic modeling study of methane, dimethyl ether, and their mixtures at high pressures, *Combust. Flame* 162 (2015) 315–330, doi:[10.1016/j.combustflame.2014.08.014](https://doi.org/10.1016/j.combustflame.2014.08.014).
- [41] K.P. Shrestha, L. Seidel, T. Zeuch, F. Mauss, Detailed kinetic mechanism for the oxidation of ammonia including the formation and reduction of nitrogen oxides, *Energy Fuels* 32 (2018) 10202–10217, doi:[10.1021/acs.energyfuels.8b01056](https://doi.org/10.1021/acs.energyfuels.8b01056).
- [42] K.P. Shrestha, L. Seidel, T. Zeuch, F. Mauss, Kinetic modeling of NO_x formation and consumption during methanol and ethanol oxidation, *Combust. Sci. Technol.* 191 (2019) 1628–1660, doi:[10.1080/00102202.2019.1606804](https://doi.org/10.1080/00102202.2019.1606804).
- [43] K.P. Shrestha, N. Vin, O. Herbinet, L. Seidel, F. Battin-Leclerc, T. Zeuch, F. Mauss, Insights into nitromethane combustion from detailed kinetic modeling – pyrolysis experiments in jet-stirred and flow reactors, *Fuel* 261 (2020) 116349, doi:[10.1016/j.fuel.2019.116349](https://doi.org/10.1016/j.fuel.2019.116349).
- [44] K.P. Shrestha, B.R. Giri, M. Adil, L. Seidel, T. Zeuch, A. Farooq, F. Mauss, Detailed chemical kinetic study of acetaldehyde oxidation and its interaction with NO_x, *Energy Fuels* 35 (2021) 14963–14983, doi:[10.1021/acs.energyfuels.1c01948](https://doi.org/10.1021/acs.energyfuels.1c01948).
- [45] K.P. Shrestha, Detailed Kinetic Modeling of Ammonia Combustion, Brandenburg University of Technology Cottbus, Senftenberg, 2021, doi:[10.26127/BTUOPEN-5709](https://doi.org/10.26127/BTUOPEN-5709).
- [46] K.P. Shrestha, B.R. Giri, A.M. Elbaz, G. Issayev, W.L. Roberts, L. Seidel, F. Mauss, A. Farooq, A detailed chemical insights into the kinetics of diethyl ether enhancing ammonia combustion and the importance of NO_x recycling mechanism, *Fuel Commun.* 10 (2022) 100051, doi:[10.1016/j.jfueco.2022.100051](https://doi.org/10.1016/j.jfueco.2022.100051).
- [47] C. Zhang, J. He, Y. Li, X. Li, P. Li, Ignition delay times and chemical kinetics of diethoxymethane/O₂/Ar mixtures, *Fuel* 154 (2015) 346–351, doi:[10.1016/j.fuel.2015.04.005](https://doi.org/10.1016/j.fuel.2015.04.005).
- [48] W. Ludwig, B. Brandt, G. Friedrichs, F. Temps, Kinetics of the reaction C₂H₅ + HO₂ by time-resolved mass spectrometry, *J. Phys. Chem. A* 110 (2006) 3330–3337, doi:[10.1021/jp0557464](https://doi.org/10.1021/jp0557464).
- [49] U. Maas, J. Warnatz, Ignition processes in hydrogen-oxygen mixtures, *Combust. Flame*. 74 (1988) 53–69, doi:[10.1016/0010-2180\(88\)90086-7](https://doi.org/10.1016/0010-2180(88)90086-7).
- [50] LOGEresearch: Combustion and chemical kinetics simulation software, (2021). <http://logesoft.com/loge-software/>.
- [51] F. Liu, O.L. Gülder, Effects of pressure and preheat on super-adiabatic flame temperatures in rich premixed methane/air flames, *Combust. Sci. Technol.* 180 (2008) 437–452, doi:[10.1080/00102200701741285](https://doi.org/10.1080/00102200701741285).
- [52] K.P. Shrestha, A.M. Elbaz, B.R. Giri, O.Z. Arab, M. Adil, L. Seidel, W.L. Roberts, A. Farooq, F. Mauss, Experimental and Kinetic Modeling Study of 1,3-Dioxolane Oxidation and Comparison with Dimethoxymethane, *Energy Fuels* 36 (2022) 7744–7754, doi:[10.1021/acs.energyfuels.2c01132](https://doi.org/10.1021/acs.energyfuels.2c01132).
- [53] J. de Vries, W.B. Lowry, Z. Serinyel, H.J. Curran, E.L. Petersen, Laminar flame speed measurements of dimethyl ether in air at pressures up to 10 atm, *Fuel* 90 (2011) 331–338, doi:[10.1016/j.fuel.2010.07.040](https://doi.org/10.1016/j.fuel.2010.07.040).
- [54] S. Jacobs, M. Döntgen, A.B.S. Alquaity, W.A. Kopp, L.C. Kröger, U. Burke, H. Pitsch, K. Leonhard, H.J. Curran, K.A. Heufer, Detailed kinetic modeling of dimethoxymethane. Part II: experimental and theoretical study of the kinetics and reaction mechanism, *Combust. Flame* 205 (2019) 522–533, doi:[10.1016/j.combustflame.2018.12.026](https://doi.org/10.1016/j.combustflame.2018.12.026).